Prandtl number dependence of stratified turbulence

Jesse D. Legaspi[1]† and Michael L. Waite[1]

[1]Department of Applied Mathematics, University of Waterloo, 200 University Avenue West, Waterloo, Ontario N2L 3G1, Canada

(Received xx; revised xx; accepted xx)

Stratified turbulence has a horizontally-layered structure with quasi-two-dimensional vortices due to buoyancy forces that suppress vertical motion. The Prandtl number Pr quantifies the relative strengths of viscosity and buoyancy diffusivity, which damp small-scale velocity and buoyancy fluctuations at different microscales. Direct numerical simulations (DNS) require high resolution to resolve the smallest flow features for large Pr. To reduce computational demand, Pr is often set to 1. In this paper, we explore how varying Pr affects stratified turbulence. DNS of homogeneous forced stratified turbulence with $0.7 \leqslant Pr \leqslant 8$ are performed for four stratification strengths and buoyancy Reynolds numbers Re_b between 0.5 and 60. Energy spectra, buoyancy flux spectra, spectral energy flux, and physical space fields are compared for scale-specific Pr-sensitivity. For $Re_b \gtrsim 10$, Pr-dependence in the kinetic energy is mainly found at scales around and below the Kolmogorov scale. The potential energy and flux exhibit more prominent Pr-sensitivity. As Re_b decreases, this Pr-dependence extends upscale. With increasing Pr, the spectra suggest eventual convergence to a limiting spectra shape at large, finite Pr, at least at scales at and above the Ozmidov scale. The Pr-sensitivity of the spectra in the most strongly stratified $Re_b < 1$ case differed from the rest, since large horizontal scales are affected by viscosity and diffusion. These findings suggest that $Pr = 1$ DNS reasonably approximate $Pr > 1$ DNS with large Re_b, as long as the focus is on kinetic energy at scales much larger than the Kolmogorov scale, but otherwise strays from $Pr > 1$ spectra around and below the Kolmogorov scale, and even upscale when $Re_b \lesssim 1$.

1. Introduction

In the turbulent flows of the atmosphere and ocean, buoyancy forces and stable stratification restrict vertical motion. At sufficiently small scales, the effects due to rotation are minor: stratification dominates these scales while Coriolis forces are weak (e.g. Riley & Lindborg 2013). Fluid velocities in stratified turbulence are approximately horizontal and layers containing quasi-two-dimensional vortices develop (e.g. Riley & Lelong 2000), along with gravity waves (e.g. Staquet & Sommeria 2002). At very small scales, fluctuations of variable fields (e.g. velocity, vorticity, density, temperature, etc.) are smoothed out by viscosity and buoyancy diffusivity, which typically occur at different inner scales. Direct numerical simulations (DNS) of stratified turbulence require that the smallest features are resolved, necessitating adequately fine grid spacing. The computational cost for these DNS is often reduced by setting the smoothing processes to be equally strong, but is done at the expense of misrepresenting the two disparate inner scales.

The relative strength of viscosity and buoyancy diffusivity is quantified by the dimen-

† Email address for correspondence: jlegaspi@uwaterloo.ca

sionless Prandtl number

$$Pr \equiv \nu/\kappa, \tag{1.1}$$

for kinematic viscosity ν and thermal diffusivity κ, with temperature as the buoyancy-influenced scalar. Typical values for Pr are 0.7 for heat in air and 7 for heat in water; for salinity in water the analogous Schmidt number for the ratio of viscosity to mass diffusivity is about 700. We use Pr in this paper to refer to this ratio. Using large Pr values for DNS is computationally expensive: since buoyancy diffusivity can be several times weaker than viscous diffusion, the smallest temperature fluctuations can be reduced to extremely small scales, demanding high spatial resolution. By setting $Pr = 1$, the equally strong viscous dissipation and buoyancy diffusivity forces the two inner scales to coincide, relaxing the need for high resolution. Stratified turbulence dynamics could be sensitive to Pr, but the $Pr \neq 1$ problem has not been studied in depth for forced homogeneous stratified turbulence with no mean shear. In this paper, we investigate the effect of varying Pr in numerical simulations of homogeneous stratified turbulence, therefore additionally evaluating the suitability for $Pr = 1$ simulations to reproduce $Pr \neq 1$ results.

Stratified turbulence is characterized by several length scales and dimensionless numbers, which we begin to review here (e.g. Riley & Lelong 2000; Riley & Lindborg 2013; Davidson 2013). The Kolmogorov microscale

$$k_d \equiv (\epsilon_k/\nu^3)^{1/4}, \tag{1.2}$$

with kinetic energy dissipation rate ϵ_k, is the inner scale of velocity fluctuations where kinetic energy is viscously dissipated into heat (Kolmogorov 1941). Analogous to the viscous dissipation scale, the temperature fluctuations, θ, have an inner scale (Corrsin 1951; Tennekes & Lumley 1972)

$$k_\theta \equiv (\epsilon_k/\kappa^3)^{1/4}, \tag{1.3}$$

for thermal diffusion. There is also the Batchelor scale for the inner scale that describes passive scalar fluctuations (Batchelor 1959; Davidson 2015),

$$k_B \equiv (\epsilon_k/\nu\kappa^2)^{1/4}. \tag{1.4}$$

These two inner temperature scales are related by

$$k_\theta/k_B = (\nu/\kappa)^{1/4} = Pr^{1/4}. \tag{1.5}$$

Depending on the size of Pr, either k_θ or k_B describes the dissipation scale for potential energy. When $Pr \lesssim 1$, k_θ is most applicable, and when $Pr \gg 1$, k_B is most applicable (Wyngaard 2010; Gotoh & Yeung 2013). When $Pr > 1$, we have that $k_\theta > k_d$, meaning that viscosity will begin to destroy velocity fluctuations at a scale where buoyancy diffusivity will not yet be effective. This subrange $k \in [k_d, k_\theta]$ is referred to as the viscous-convective subrange. If $Pr \gg 1$, theory suggests that in the viscous-convective subrange, the potential energy spectrum has the form

$$E_P \sim \epsilon_p(\epsilon_k/\nu)^{-1/2}k^{-1}, \tag{1.6}$$

with potential energy dissipation rate ϵ_p, as predicted by Batchelor (1959). In the opposite case when $Pr < 1$, buoyancy diffusivity will act on small scales where viscous effects are not yet significant, and the subrange $k \in [k_\theta, k_d]$ is the inertial-diffusive subrange (Wyngaard 2010). In the atmosphere, these inner scales typically correspond to lengths on the order of millimeters.

The buoyancy frequency N characterizes stratification strength: for temperature stratification,

$$N^2 \equiv \frac{g}{\theta_0}\beta, \tag{1.7}$$

where g is gravitational acceleration, θ_0 is a reference temperature, and β is the background potential temperature gradient (e.g. Kundu *et al.* 2012). The potential energy dissipation rate can be related to the diffusion of temperature fluctuations by

$$\epsilon_p = \frac{g/\theta_0}{\beta}\kappa\overline{\frac{\partial\theta}{\partial x_j}\frac{\partial\theta}{\partial x_j}}, \tag{1.8}$$

where $\overline{(\cdot)}$ denotes a mean quantity.

The $Pr \neq 1$ problem in strongly stratified turbulence becomes complicated by the horizontally-layered structure of the flow. In stratified turbulence, quasi-two-dimensional vortices become thinner with stronger stratification (Billant & Chomaz 2001), introducing additional small scales that must be adequately resolved in DNS. The horizontal Froude number

$$Fr_h = U/NL_h, \tag{1.9}$$

for rms velocity U and horizontal length scale L_h, is a dimensionless number that quantifies stratification strength in stratified turbulence (Billant & Chomaz 2001; Brethouwer *et al.* 2007). While turbulence is characterized by a large Reynolds number

$$Re = UL_h/\nu, \tag{1.10}$$

stratified turbulence can fall into one of two regimes depending on its buoyancy Reynolds number (Smyth & Moum 2000; Riley & de Bruyn Kops 2003; Brethouwer *et al.* 2007)

$$Re_b = ReFr_h^2. \tag{1.11}$$

Typical mesoscale flows (e.g. squall lines and sea breezes) have tropospheric values $U \sim 1$ ms^{-1}, $L_h \sim 1$–100 km, $N \sim 10^{-2}$ s^{-1}, and $\nu \sim 10^{-5}$ m^{2}s^{-1}, giving ranges of dimensionless numbers $Fr_h \sim 10^{-3}$–10^{-1}, $Re \sim 10^8$–10^{10}, and $Re_b \sim 10^4$–10^6 (e.g. Lilly 1983; Waite 2013). From the approximation $\epsilon_k \sim U^3/L_h$ (e.g. Taylor 1935; Lindborg 2006), these values give a corresponding $\epsilon_k \sim 10^{-5}$–10^{-3} m^{2}s^{-3} (similar to dissipation values in the stratosphere, e.g. Dewan 1997).

Stratified turbulence also has the buoyancy scale

$$k_b \equiv N/U, \tag{1.12}$$

and Ozmidov scale

$$k_O \equiv (N^3/\epsilon_k)^{1/2}, \tag{1.13}$$

which characterize different small-scale processes in the flow. The thickness of the horizontal layers in stratified turbulence, and thus the largest vertical overturning scale corresponds to k_b (Carnevale *et al.* 2001; Billant & Chomaz 2001; Waite & Bartello 2004). The Ozmidov scale is the largest scale for which the flow resembles small-scale three-dimensional isotropic turbulence (Ozmidov 1965). Whether k_O is upscale or downscale of the dissipation range depends on the regime of stratified turbulence, such that

$$k_d/k_O \sim Re_b^{3/4}, \tag{1.14}$$

using the $\epsilon_k \sim U^3/L_h$ assumption (Lindborg 2006; Maffioli & Davidson 2016).

Past investigations that set $Pr = 1$ revealed important properties of stratified turbulence and confirmed various scaling arguments. Stratified turbulence has two regimes:

on the scale of the thickness of the quasi-two-dimensional vortices, viscosity may be weak enough that small eddies may emerge and the layers are turbulently coupled (characterized by $Re_b > 1$), or viscosity may be strong enough that the layers are non-turbulent and become viscously coupled (characterized by $Re_b < 1$) (Riley & de Bruyn Kops 2003; Brethouwer *et al.* 2007). Within the horizontal layers, Kelvin-Helmholtz (KH) instabilities emerge when $Re_b \gtrsim 1$ and break down into small-scale turbulence (Lilly 1983; Riley & de Bruyn Kops 2003; Laval *et al.* 2003; Brethouwer *et al.* 2007; Waite 2011). The kinetic and potential energy spectra in terms of horizontal wavenumber k_h and vertical wavenumber k_v have been extensively examined in studies with stratified turbulence simulations. Forced simulation results have shown the horizontal kinetic and potential energy spectra to exhibit $k_h^{-5/3}$ scaling (Brethouwer *et al.* 2007; Almalkie & de Bruyn Kops 2012). In some instances, there is a noticeable bump at $k_h \sim k_b$ due to KH instabilities (Laval *et al.* 2003; Brethouwer *et al.* 2007; Waite 2011). In the limit of strong stratification, the one-dimensional horizontal wavenumber spectra for kinetic and potential energy (where k_h is the wavenumber magnitude in either the x- or y-direction, as in Lindborg & Brethouwer 2007) resemble:

$$E_K(k_h) = C_1 \epsilon_k^{2/3} k_h^{-5/3}, \tag{1.15}$$

$$E_P(k_h) = C_2 \frac{\epsilon_p}{\epsilon_k^{1/3}} k_h^{-5/3}, \tag{1.16}$$

where C_1 and C_2 are the Kolmogorov and Obukhov-Corrsin constants. The present work uses the two-dimensional horizontal wavenumber: the corresponding constants for the two-dimensional spectra, C_1' and C_2', are related to the one-dimensional values by $C' \approx 1.40C$, for which Lindborg (2006) and Brethouwer *et al.* (2007) use $C_1' = C_2' = 0.71$ as a reference value for their simulation results.

Scaling arguments have suggested k_v^{-3} scaling for the vertical kinetic and potential energy spectra for a limited range of wavenumbers (Billant & Chomaz 2001; Lindborg 2006); simulations have exhibited similarly steep vertical spectra past k_b (Waite & Bartello 2004; Brethouwer *et al.* 2007; Almalkie & de Bruyn Kops 2012). The behaviour of vertical spectra is scale-dependent: at large horizontal scales, agreement with k_v^{-3} scaling was shown for both kinetic and potential energy, but for different ranges of wavenumbers in simulations forced at large scales (Maffioli 2017). Decaying simulations also supported the horizontal $k_h^{-5/3}$ scaling for kinetic and potential energy found in forced simulations (Bartello & Tobias 2013; Maffioli & Davidson 2016), and were not influenced by stratification strength for large Re (Lindborg 2006; Bartello & Tobias 2013). The conversion from potential to kinetic energy can be quantified by the buoyancy flux term in the energy budget (Holloway 1988; Waite 2014). In the buoyancy flux spectrum, restratification describes the small-scale subrange with positive buoyancy flux, where potential energy is converted to vertical kinetic energy, restratifying the flow (Holloway 1988; Bouruet-Aubertot *et al.* 1996; Carnevale *et al.* 2001). The relationship between the characteristic wavenumbers and spectral scaling laws is summarized in figure 1.

Stratified turbulence with $Pr > 1$ has not been as well-studied as the $Pr = 1$ case, but previous studies have analyzed such simulations with some compromises in other simulation parameters. Comparisons of decaying stratified turbulence DNS with $Pr = 7$ and $Pr = 700$ revealed Pr-dependence in the energy spectra (Okino & Hanazaki 2017, 2019, 2020). The $Pr = 700$ potential energy spectra initially exhibited k^{-1} scaling at large wavenumbers (as predicted in the viscous-convective subrange for passive scalars (Batchelor 1959)), and by the final decay period, a flat spectrum developed in the dissipation range. However, the initial Reynolds number in this study was necessarily

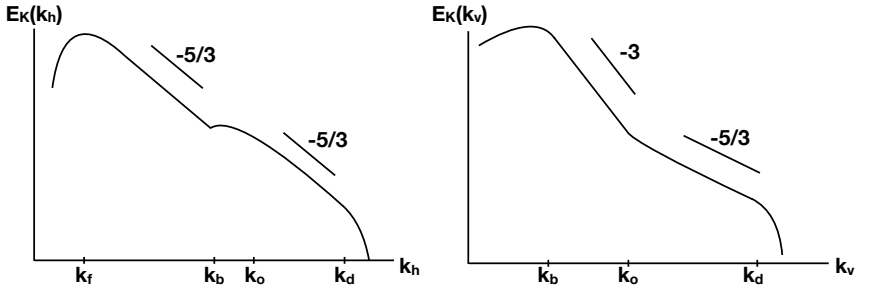

FIGURE 1. A schematic diagram of the expected spectral scaling laws and characteristic wavenumbers for stratified turbulence with $Fr_h \ll 1$, $Re_b \gg 1$, and $Pr = 1$.

small (initial $Re_0 = 50$) to accommodate the very large Pr, limiting the extent of the inertial range; while small-scale changes due to Pr have been identified, it is also of interest to determine any possible Pr-dependence upscale of the dissipation range. In Okino & Hanazaki (2019), more DNS of decaying stratified turbulence were performed with a larger initial Reynolds number $Re_0 = 100$ (corresponding to a microscale Reynolds number of $Re_\lambda = 42$) for $Pr = 1$, 7, and 70. Each decaying DNS had an initial buoyancy Reynolds number of about 50 which quickly dropped to $Re_b \sim 1$ within the first quarter of the simulation. A k^{-1} power law region is again observed in the horizontal and vertical potential energy spectra for the largest Pr (70 in this study) early in the simulation before any significant decay. The authors note less of a difference in kinetic energy spectra between $Pr = 7$ and $Pr = 70$ than the difference between $Pr = 1$ and $Pr = 7$. An older study which performed DNS of stably stratified homogeneous turbulent shear flow concluded higher-Pr flows were more likely to exhibit counter-gradient heat flux (i.e. restratification) in the vertical direction, but their moderate Re limits its applicability to geophysical flows (Gerz *et al.* 1989). Another study where DNS of density-stratified turbulent wakes were performed for $Pr = 0.2$, 1, and 7 concluded that using the $Pr = 1$ case to approximate the $Pr = 7$ case was reasonable, though the grid spacing was four times the smallest length scale of the flow (de Stadler *et al.* 2010). The $Pr = 7$ case induced small-scale changes with little influence on the wake's large-scale features, and the differences between the $Pr = 1$ and $Pr = 7$ cases were small compared to the substantial difference in computational costs. Mixing efficiency, which is often studied in DNS with $Pr = 1$ (e.g. Caulfield & Peltier 2000; Maffioli *et al.* 2016; Howland *et al.* 2020), has been found to decrease with increasing Pr (Smyth *et al.* 2001; Stretch *et al.* 2010; Salehipour *et al.* 2015). In comparison, the dependence of mixing efficiency on stratification strength and the Richardson number is more complicated (Peltier & Caulfield 2003; Howland *et al.* 2020).

In this work, we address the following question: in DNS of stratified turbulence with $Fr_h < 1$, are the dynamics at scales on the order of the Ozmidov and Kolmogorov scales and larger independent of Pr for $Re_b \sim O(10)$? Or put another way: are DNS with $Pr = 1$ able to reproduce results with $Pr > 1$, at least at large scales? Many DNS studies of stratified turbulence consider $Re_b \lesssim O(10)$, especially with strong stratification (e.g. Kimura & Herring 2012; Bartello & Tobias 2013; Maffioli 2017; Okino & Hanazaki 2019), and many of these studies set $Pr = 1$; answering this question will shed light on the applicability of their results to $Pr > 1$ flows. Since varying Pr affects the relative strengths of small-scale processes, we anticipate that most Pr-induced changes will occur around the small viscous dissipation and buoyancy diffusion scales. If the viscosity is held fixed while Pr is increased, we would also predict that changes in the temperature and potential energy would be more pronounced than in the velocity and

kinetic energy. Further, for fixed viscosity, the dissipation of potential energy (or of temperature fluctuations, as in equation (1.8)) is expected to be especially Pr-sensitive as k_B is modified. Equation (1.14) expresses a scale separation in stratified turbulence in terms of the characteristic Re_b, suggesting that sensitivity to Pr may depend on the regime of stratified turbulence. Indeed, for $Re_b \lesssim 1$, stratified turbulence is dominated by large, thin, viscously coupled layers, and therefore large horizontal scales are affected directly by viscous dissipation (e.g. Brethouwer *et al.* 2007) and may be sensitive to Pr. As a small-scale phenomenon involving potential energy, restratification is another candidate for Pr-dependence. Due to the complicated dependence of buoyancy flux on the stratification strength, varying Pr may also affect the restratification range in regime-specific ways (Lucas *et al.* 2017).

In this paper, DNS of homogeneous forced stratified turbulence are performed and analyzed to explore the effect of varying Pr on flow dynamics. The choices of Pr and stratification span a range of Re_b so that the $Re_b = 1$ stratified turbulence regime transition may also be studied. In section 2, the numerical model, equations, and setup of simulations are explained. In section 3, the simulation results are analyzed in terms of scale-specific observations of Pr-dependence in the energy spectra, buoyancy flux spectra, spectral energy flux, and snapshots of physical space fields. Conclusions, discussion, and future work are given in section 4.

2. Methods

2.1. *Equations and model*

For the stratified turbulence simulations presented here, the governing equations are the incompressible uniformly stratified non-rotating Boussinesq equations in three dimensions:

$$\frac{\mathrm{D}\boldsymbol{u}}{\mathrm{D}t} = -\nabla p + \alpha\theta\hat{\boldsymbol{z}} + \boldsymbol{F}_u + \nu\nabla^2\boldsymbol{u}, \tag{2.1}$$

$$\frac{\mathrm{D}\theta}{\mathrm{D}t} + \beta w = F_b + \kappa\nabla^2\theta, \tag{2.2}$$

$$\nabla\cdot\boldsymbol{u} = 0, \tag{2.3}$$

where $\boldsymbol{u}$ is velocity, p is pressure scaled by a reference density, θ is the potential temperature fluctuation (or negative density fluctuation), $\hat{\boldsymbol{z}}$ is the upward vertical unit vector, $\boldsymbol{F}_u$ is the velocity forcing, F_b is the temperature forcing, ν is viscosity, κ is diffusivity, α is thermal expansivity, and β is the background potential temperature gradient (Herring & Métais 1989).

The DNS code computes the fluid velocity by first solving for vorticity ($\boldsymbol{\omega} = \nabla\times\boldsymbol{u}$) from the vorticity formulation of (2.1):

$$\frac{\partial\boldsymbol{\omega}}{\partial t} = \nabla\times(\boldsymbol{u}\times\boldsymbol{\omega}) + \alpha\begin{bmatrix}\partial\theta/\partial y\\ -\partial\theta/\partial x\\ 0\end{bmatrix} + \boldsymbol{F}_\omega + \nu\nabla^2\boldsymbol{\omega} \tag{2.4}$$

and (2.2), then inverting the result for $\boldsymbol{u}$. This inversion assumes no mean velocity. In this formulation, the second term on the right hand side of (2.4) corresponds to the baroclinic generation of vorticity, and $\boldsymbol{F}_\omega = \nabla\times\boldsymbol{F}_u$ is the vorticity forcing.

The spectral transform method is used on a triply periodic domain to solve the uniformly stratified Boussinesq equations (2.2), (2.3), and (2.4). The domain is a cube of size $L\times L\times L$ and grid size $n\times n\times n$ in both the physical and Fourier domains where $\boldsymbol{u}$, $\boldsymbol{\omega}$, and θ are stored. Nonlinear terms are computed in the physical domain, and

spatial derivatives are computed in the Fourier domain, and a Fast Fourier Transform is used to go between domains (Frigo & Johnson 2005). Third-order Adams-Bashforth time stepping is used with constant time step Δt, and viscous and diffusive terms use a Crank-Nicolson scheme (Durran 2010). Aliasing issues are countered by a less restrictive wavenumber truncation than the 2/3 rule, which is known to eliminate all aliasing error (Durran 2010). Previous DNS studies have used wavenumber truncations as high as 15/16, which still managed to remove the dominant aliasing error (Riley & de Bruyn Kops 2003). In the following simulations, the Fourier coefficients are cubically truncated at a maximum wavenumber $k_{max} = (\frac{n}{2})(\frac{8}{9}) = 4n/9$. The effective resolution is then $\Delta x = \Delta y = \Delta z = 9L/8n$ with wavenumber spacing $\Delta k_x = \Delta k_y = \Delta k_z = 2\pi/L$. This model has been used in numerous studies of stratified turbulence, e.g. Waite (2011, 2017); Lang & Waite (2019).

The equations for the kinetic and potential spectral energy budget for each wavevector $\boldsymbol{k}$ are (e.g Wyngaard 2010; Riley & Lindborg 2013):

$$\frac{\partial E_K}{\partial t}(\boldsymbol{k}) = T_K(\boldsymbol{k}) + B(\boldsymbol{k}) - D_K(\boldsymbol{k}) + F(\boldsymbol{k}), \tag{2.5}$$

$$\frac{\partial E_P}{\partial t}(\boldsymbol{k}) = T_P(\boldsymbol{k}) - B(\boldsymbol{k}) - D_P(\boldsymbol{k}). \tag{2.6}$$

The first terms on the right hand side of (2.5)-(2.6),

$$T_K(\boldsymbol{k}) \equiv -\mathrm{Im} \sum_{\boldsymbol{k}+\boldsymbol{p}+\boldsymbol{q}=0} P_{ijm}(\boldsymbol{k})\hat{u}_j(\boldsymbol{p})\hat{u}_m(\boldsymbol{q})\hat{u}_i(\boldsymbol{k}), \tag{2.7}$$

$$T_P(\boldsymbol{k}) \equiv -\frac{\alpha}{\beta}\mathrm{Im}\left(k_j \sum_{\boldsymbol{k}+\boldsymbol{p}+\boldsymbol{q}=0} \hat{\theta}(\boldsymbol{k})\hat{\theta}(\boldsymbol{p})\hat{u}_j(\boldsymbol{q}) \right), \tag{2.8}$$

are the nonlinear kinetic and potential energy transfer respectively, using the standard projection operator P_{ijm} (e.g. Rose & Sulem 1978). The spectral buoyancy flux, B, is

$$B(\boldsymbol{k}) \equiv \alpha \mathrm{Re}\Big(\hat{\theta}(\boldsymbol{k})\hat{w}^*(\boldsymbol{k})\Big), \tag{2.9}$$

the kinetic and potential energy dissipation are

$$D_K(\boldsymbol{k}) \equiv 2\nu k^2 E_K(\boldsymbol{k}), \tag{2.10}$$

$$D_P(\boldsymbol{k}) \equiv 2\kappa k^2 E_P(\boldsymbol{k}), \tag{2.11}$$

and F is the forcing. Horizontal and vertical wavenumber spectral budgets are found from (2.5-2.6) by summing over all wavevectors $\boldsymbol{k}$ for particular horizontal wavenumber k_h or vertical wavenumber k_v.

The spectral buoyancy flux B is the cross spectrum of buoyancy and vertical velocity, and can be interpreted as the transfer of potential to kinetic energy (e.g. Holloway 1988). Holloway (1988) suggested that restratification, i.e. positive B at small scales, occurs because the downscale transfer of potential energy to small scales was more efficient than for kinetic energy, leading to a tendency for more potential energy than kinetic energy to accumulate at small scales. Oppositely, when only kinetic energy is forced, more kinetic energy would accumulate at large scales than potential energy, and so these imbalances drive the conversion of kinetic to potential energy at large scales ($B < 0$) and potential to kinetic energy at small scales ($B > 0$, restratification).

The transfer terms represent the conservative transfer of potential and kinetic energy to different wavenumbers. Since they are conservative, the spectral fluxes of kinetic and

Run	Pr	Fr_h	Fr_f	Re	Re_f	Re_b	ϵ_k	ϵ_p	ϵ_p/ϵ_k	k_d	k_B	k_{max}/k_d	k_{max}/k_B	k_O	k_b
A0	0.7	0.0911	0.46	3310	286	27.5	0.718	0.395	0.550	181	151	3.77	4.50	15	5
A1	1	0.0947	0.46	3197	286	28.7	0.750	0.379	0.505	183	183	3.73	3.73	15	5
A2	2	0.0983	0.46	3094	286	29.9	0.783	0.335	0.427	185	261	3.69	2.61	14	5
A3	4	0.103	0.46	2941	286	31.2	0.816	0.306	0.374	187	374	3.65	1.83	14	5
A4	8	0.106	0.46	2839	286	31.7	0.829	0.276	0.333	188	531	3.64	1.29	14	5
A1h	1	0.0884	0.46	6554	571	52.0	0.681	0.359	0.527	300	300	2.84	2.84	16	5
A4h	8	0.0955	0.46	6197	571	56.5	0.740	0.294	0.398	307	867	2.78	0.98	15	5
B0	0.7	0.0402	0.23	4304	286	6.94	0.727	0.397	0.547	181	152	3.76	4.49	42	9
B1	1	0.0420	0.23	4130	286	7.28	0.762	0.357	0.468	184	184	3.71	3.71	41	8
B2	2	0.0452	0.23	3877	286	7.92	0.829	0.296	0.357	188	265	3.64	2.57	40	8
B3	4	0.0479	0.23	3658	286	8.38	0.877	0.243	0.277	190	380	3.59	1.79	39	8
B4	8	0.0499	0.23	3491	286	8.71	0.911	0.205	0.225	192	543	3.55	1.26	38	8
C0	0.7	0.0191	0.12	5279	286	1.93	0.808	0.401	0.496	186	156	3.66	4.37	114	16
C1	1	0.0201	0.12	5041	286	2.03	0.850	0.352	0.414	189	189	3.61	3.61	111	16
C2	2	0.0218	0.12	4670	286	2.22	0.930	0.267	0.287	193	273	3.53	2.50	106	16
C3	4	0.0233	0.12	4381	286	2.37	0.993	0.199	0.201	196	392	3.48	1.74	103	16
C4	8	0.0244	0.12	4179	286	2.49	1.041	0.149	0.143	199	562	3.43	1.21	100	16
D0	0.7	0.00896	0.058	6737	286	0.541	0.907	0.344	0.380	192	160	3.56	4.25	304	29
D1	1	0.00935	0.058	6485	286	0.567	0.949	0.302	0.319	194	194	3.52	3.52	297	29
D2	2	0.0101	0.058	6045	286	0.613	1.026	0.221	0.216	198	280	3.45	2.44	286	29
D3	4	0.0107	0.058	5674	286	0.654	1.094	0.153	0.134	201	402	3.39	1.70	277	29
D4	8	0.0112	0.058	5423	286	0.684	1.145	0.102	0.0889	203	575	3.35	1.19	270	29

TABLE 1. Simulation parameters, nondimensional numbers, and wavenumbers for all simulations. The run label letter A/B/C/D indicates a common stratification strength. The run label number 0/1/2/3/4 indicates a common Prandtl number. All simulations have the same viscosity, resolution, and maximum wavenumber: $\nu = 0.12$ cm^2/s, $n = 1536$, $k_{max} = 682$ with the exception of runs A1h and A4h where $\nu = 0.06$ cm^2/s, $n = 1920$, $k_{max} = 853$. Wavenumbers are nondimensionalized by $2\pi/L$; energy dissipation is nondimensionalized by forcing power P.

potential energy are obtained from the transfer terms as

$$\Pi_K(k) = -\int_0^k T_K(k)\ \mathrm{d}k, \tag{2.12}$$

$$\Pi_P(k) = -\int_0^k T_P(k)\ \mathrm{d}k, \tag{2.13}$$

where k can be the isotropic, horizontal, or vertical wavenumber magnitude. As conserved quantities, the transfer terms satisfy

$$\int_0^\infty T_K(k)\ \mathrm{d}k = 0, \tag{2.14}$$

$$\int_0^\infty T_P(k)\ \mathrm{d}k = 0, \tag{2.15}$$

which also manifest as $\Pi_K = 0$ and $\Pi_P = 0$ at k_{max}.

2.2. *Simulation setup*

The parameter values, nondimensional numbers, and wavenumbers for all simulations presented here are given in Table 1 and described here. Most simulations are performed on cubic domains with $n = 1536$ grid points in each direction. Two additional higher-resolution simulations, A1h and A4h, use $n = 1920$.

Large-scale vortical motion is excited by directly forcing vortical modes, i.e. flow with rotational horizontal velocity and no vertical velocity (vortical mode forcing was also used by e.g. Waite & Bartello 2004; Lindborg 2006; Brethouwer *et al.* 2007). Gravity waves are not directly forced. Time dependence of the forcing follows an AR(1) red noise process with a short decorrelation time scale $\tau =$ of 10 time steps (i.e. nearly white noise, e.g. Waite 2017),

$$G(\boldsymbol{k}, t_n) = \tilde{\alpha} G(\boldsymbol{k}, t_{n-1}) + \tilde{\beta} g(\boldsymbol{k}, n), \tag{2.16}$$

for a random complex number $g(\boldsymbol{k}, n)$. The random number's real and imaginary parts follow a Gaussian distribution with a mean of 0 and variance of 1. The coefficients in equation (2.16) satisfy

$$\tilde{\alpha} = \exp(-\Delta t/\tau), \tilde{\beta}^2 = 1 - \tilde{\alpha}^2. \tag{2.17}$$

A specified forcing amplitude $A(\boldsymbol{k})$ multiplies $G(\boldsymbol{k}, t_n)$ and is nonzero only in the spherical shell $k \in [3, 5]$ centred on forcing wavenumber $k_f = 4$. The amplitude is given by

$$A(\boldsymbol{k}) = \begin{cases} a(k_f + 1 - |\boldsymbol{k}|)(|\boldsymbol{k}| - k_f + 1) & , \quad k_f - 1 \leqslant |\boldsymbol{k}| \leqslant k_f + 1, \\ 0 & , \quad ||\boldsymbol{k}| - k_f| > 1. \end{cases} \tag{2.18}$$

The forcing injects kinetic energy only. The time-averaged rate of energy injection by the forcing is approximately determined by the forcing amplitude as

$$P = 2\tau \sum_{\boldsymbol{k}} A(\boldsymbol{k})^2, \tag{2.19}$$

(see Waite 2017, who found that the time averaged energy injection rate scaled like P when τ was short). Note, this forcing approach is different from that employed by Lindborg (2006), in which the instantaneous, not time-averaged, energy injection rate is fixed. The simulations are initialized with a prescribed kinetic and potential energy at a chosen wavenumber $k = 3$. Damping is applied to the $k_h = 0$ modes to prevent the accumulation of energy in vertically sheared horizontal flow (Smith & Waleffe 2002). More details on the code used for these simulations can be found in past studies (Waite 2011, 2017).

The simulations are described with dimensional parameters L, ν, N, etc. as well as dimensionless parameters. The dimensional parameters are chosen to be broadly similar to laboratory values following Waite (2014): L is set to be 2π metres for convenience, and the forcing amplitude is chosen to give velocities on the order of 1 cm/s and energy dissipation rates on the order of 0.01 cm^2/s^3. The forcing amplitude is the same in all simulations, and gives $P = 0.02586$ cm^2/s^3, which yields a forcing eddy time scale of $T_f = P^{-1/3} k_f^{-2/3}$. Stratification is changed by varying N. Viscosity is fixed at $\nu = 0.12$ cm^2/s in all simulations except for A1h and A4h. The quantities in table 1 are nondimensionalized by P and k_f as in Lindborg (2006). Energy time series, energy dissipation time series, energy spectra, and energy transfer spectra computed for each simulation are nondimensionalized by P and k_f. A Froude number can be defined from the forcing parameters: $Fr_f = (Pk_f^2)^{1/3}/N$ (note that we use k_f, not $k_f/2\pi$, so our Fr_f values are larger at the same stratification than those used by Lindborg 2006). This forcing Froude number Fr_f is reported in table 1 ($Fr_f = 0.46$, 0.23, 0.12, 0.058) in

place of our dimensional N values ($N = 0.075$ s^{-1}, 0.15 s^{-1}, 0.3 s^{-1}, 0.6 s^{-1}). A forcing Reynolds number, $Re_f = P^{1/3}/\nu k_f^{4/3}$, is also reported in table 1. The total dissipation rate $\epsilon_k + \epsilon_p$ is approximately equal to (but slightly larger than) P in all cases, consistent with Waite (2017), who found that the actual energy injection rate was a little larger than (1.1 times) that determined by the forcing amplitude.

The total integration length for all simulations corresponds to approximately 17.3 forcing eddy timescales, and the time step is $\Delta t/T_f = 0.000216$. Time series are used for the calculated values in Table 1, based on values for ϵ_k and ϵ_p averaged over $t/T_f \in [10.4, 17.3]$. The length scale used in Fr_h and Re is computed from $L_h = U^3/\epsilon_k$, where U is the root mean square velocity (as in Brethouwer *et al.* 2007). While questions have been raised about the appropriateness of this L_h in stratified turbulence (e.g. Maffioli & Davidson 2016), we include the corresponding Fr_h for comparison with other studies that used it. Velocity, vorticity, and temperature fields in physical space are output at equidistant times over the integration length (either 5 or 9 output times depending on the case).

The first set of simulations has a fixed stratification, thus setting Fr_f, and separate trials for each Prandtl number. This approach was repeated for a total of 4 stratification strengths and 5 Prandtl numbers, resulting in 20 simulations at the same resolution with $Pr = 0.7$, 1, 2, 4, and 8 (runs with labels 0, 1, 2, 3, and 4 respectively) and $Fr_f = 0.46$, 0.23, 0.12, and 0.058 (runs with labels A, B, C, and D respectively). The stratification strengths were chosen to give a range of Fr_h, and values for Re_b of $O(1)$ and larger. The resolution $n = 1536$ ensures that the Kolmogorov and Batchelor scales are resolved ($k_{max}/k_d \approx 3$ and $k_{max}/k_B > 1$). While the forcing amplitude and viscosity are fixed in all the $n = 1536$ runs, the mixing efficiency depends on Fr_f and Pr. As a result, ϵ_k and k_d are also slightly dependent on Fr_f and Pr. In addition to studying dependence on Pr, these parameter values explore both regimes of strongly stratified turbulence, $Re_b < 1$ and $Re_b > 1$. Two additional simulations, A1h and A4h, have the same stratification but larger Re and Re_b than the other A cases, and are discussed in section 3.3.

The horizontal and vertical kinetic energy spectra are (e.g. Waite & Bartello 2004)

$$E_K(k_h)\delta = \frac{1}{2} \sum_{\boldsymbol{k'} \in I_h(k_h)} |\hat{\boldsymbol{u}}(\boldsymbol{k'})|^2, \tag{2.20}$$

$$E_K(k_v)\delta = \frac{1}{2} \sum_{\boldsymbol{k'} \in I_v(k_v)} |\hat{\boldsymbol{u}}(\boldsymbol{k'})|^2, \tag{2.21}$$

where

$$I_h(k_h) = \{\boldsymbol{k'} \mid k_h - \delta/2 \leqslant k'_h < k_h + \delta/2\}, \tag{2.22}$$

$$I_v(k_v) = \{\boldsymbol{k'} \mid k_v - \delta/2 \leqslant |k'_v| < k_v + \delta/2\}, \tag{2.23}$$

$\delta = 2\pi/L$, and $\hat{\boldsymbol{u}}$ corresponds to the velocity in the Fourier domain. The horizontal and vertical potential energy spectra are similarly defined:

$$E_P(k_h)\delta = \frac{1}{2} \sum_{\boldsymbol{k'} \in I_h(k_h)} |\hat{b}(\boldsymbol{k'})|^2/N^2, \tag{2.24}$$

$$E_P(k_v)\delta = \frac{1}{2} \sum_{\boldsymbol{k'} \in I_v(k_v)} |\hat{b}(\boldsymbol{k'})|^2/N^2, \tag{2.25}$$

where $\hat{b}$ corresponds to the buoyancy in the Fourier domain.

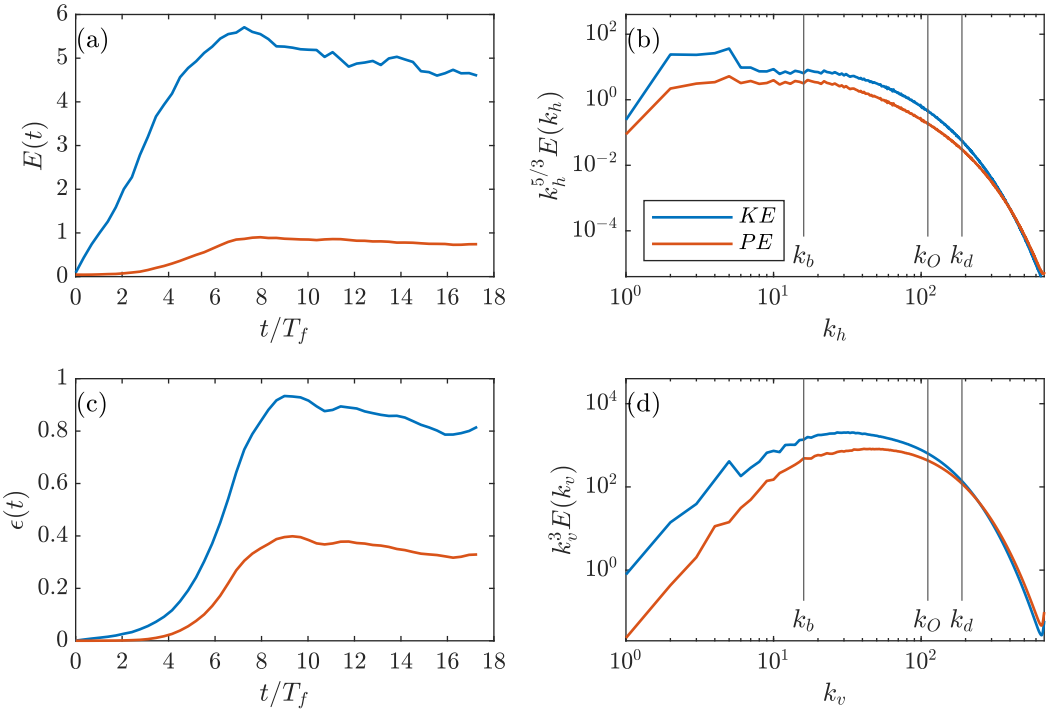

FIGURE 2. Energy spectra and time series for run C1: $Pr = 1$, $Fr_f = 0.12$. Left column: time series of (a) kinetic and potential energy and (c) energy dissipation. Right column: compensated kinetic and potential energy spectra in terms of (b) horizontal and (d) vertical wavenumber. Characteristic wavenumbers k_b, k_O, and k_d are denoted with vertical solid lines. Note that k_B is coincident with k_d for $Pr = 1$.

3. Results

In this section, we analyze kinetic and potential energy spectra, spectral budget terms, and physical space fields of the simulations. We start with $Pr = 1$, first focusing on the $Fr_f = 0.12$ case (section 3.1.1), then we look at the effect of varying Fr_f for the $Pr = 1$ cases (section 3.1.2). In section 3.2 we analyze the spectra and snapshots for Pr-dependence. In section 3.3 we briefly discuss the effect of further increasing Re_b on the present results.

3.1. *Overview of $Pr = 1$ cases*

3.1.1. *Overview of the $Fr_f = 0.12$, $Pr = 1$ case*

We start with an overview of the $Pr = 1$ case with intermediate stratification $Fr_f = 0.12$ (run C1). Time series of kinetic and potential energy and dissipation are plotted in figure 2(a,c). The energy and dissipation rates increase for the first 8 forcing timescales until the flow develops into statistically stationary turbulence, after which these quantities equilibrate. The energy and dissipation plots are fairly steady for $t/T_f \in [10.4, 17.3]$, which is chosen as the time averaging interval. Approximate stationarity at these times is observed for all the simulations, so the same time averaging interval is used for all cases.

Compensated horizontal and vertical wavenumber spectra are plotted in figure 2(b,d) (the full wavenumber energy spectra are omitted as they closely resemble the vertical spectra). Spikes in the kinetic energy spectra for small wavenumbers are a consequence of the large-scale forcing for $k \in [3, 5]$. For $Pr = 1$, k_d and k_B (label omitted) are

coincident. Beyond the forcing interval, the horizontal spectra are close to the expected $k_h^{-5/3}$ scaling law (Lindborg 2006, represented by a plateau in the compensated spectra) for less than one decade, as expected for $Re_b = 2.03$. The uncompensated vertical kinetic energy spectrum is flat out to k_b (not pictured in figure 2 but can be deduced by the approximate slope of +3 in the compensated plots), while the potential energy spectrum is peaked at k_b. Beyond k_b, the vertical spectra steepens to approximately k_v^{-3}, appearing as a short plateau in the compensated plot. Due to the modest $Re_b = 2.03$ in this case, there is only a small separation between the Ozmidov and dissipation scales. Since $Pr = 1$, the kinetic and potential energy are expected to behave similarly at very small scales as both momentum- and buoyancy-diffusive scales are equivalent; indeed, in the dissipation range beyond k_d (or k_B), the spectra are nearly the same.

Figure 3 shows vertical and horizontal slices of horizontal velocity and vorticity at the end of the simulation. With $Re_b = 2.03$ and $Fr_h = 0.019$, run C1 is in the strongly stratified and slightly viscous regime where the flow is arranged into layers of pancake eddies. This run is only slightly past the $Re_b = 1$ transition from viscously to turbulently coupled layers. In figures 3(a,b), the layerwise arrangement and intermittent small-scale Kelvin-Helmholtz (KH) instabilities can be seen clearly in the vertical slices of the velocity and y-component vorticity fields. The buoyancy wavenumber $k_b = 16$ for run C1 is approximately the number of layers in the flow. Since the thickness of the horizontal layers in stratified turbulence is set by the buoyancy length scale L_b (Billant & Chomaz 2001; Waite & Bartello 2004), the corresponding wavenumber $k_b = N/U = 2\pi/L_b$ is approximately the number of layers in our domain of height 2π. The horizontal slices of velocity and z-component vorticity fields in figures 3(c,d) clearly show the signature of the large-scale vortical forcing. In addition, small horizontal scales associated with KH billows are visible in figure 3(d).

The potential energy dissipation field (equation (1.8)) is shown in figure 4. Run C1 has few regions that are highly dissipative, and in figure 4(a) the dissipative regions resemble small quasi-horizontal features in contrast with the intermittent worms expected in unstratified homogeneous 3D turbulence (e.g. Burgers 1948; Siggia 1981; Ishihara *et al.* 2013). These dissipative regions also appear to be arranged in horizontal layers (figure 4(b)), like the vertical slices of u and ω_y in figure 3(a,b).

We now consider the spectral budget for run C1. The spectra of T_K, T_P, D_K, D_P, and B from the energy budget (2.5)-(2.6) are plotted for run C1 in figure 5(a,b). Excluding the dissipation terms, the horizontal and vertical spectral budgets are similar at large scales; the shape of the spectra at small wavenumbers is primarily influenced by the large-scale forcing. In the forcing interval, there is substantial transfer of the injected kinetic energy out of the forced wavenumbers, as indicated by large negative spikes in $T_K(k_h)$ and $T_K(k_v)$. The potential energy budget terms $T_P(k_h)$, $T_P(k_v)$, $B(k_h)$ and $B(k_v)$ are very small and negative in this range, indicating that, while there is no direct forcing of potential energy, there is some conversion of the remaining injected kinetic energy to potential energy.

In the horizontal spectral budget, downscale of the forcing interval, $T_K(k_h)$ is positive and has a small peak at k_b. Some of the kinetic energy deposited at these wavenumbers is converted to potential energy, as indicated by the negative buoyancy flux in this range. Indeed, between the forcing interval and k_b, $T_P(k_h)$ and $B(k_h)$, both of which are negative, increase to near zero. The dissipation spectra in this range reveals that much of the energy going into these horizontal scales is lost to dissipation: dissipation at large and intermediate horizontal scales can occur at large Re through the vertical part of the dissipation term, which is restricted to small vertical scales but not necessarily

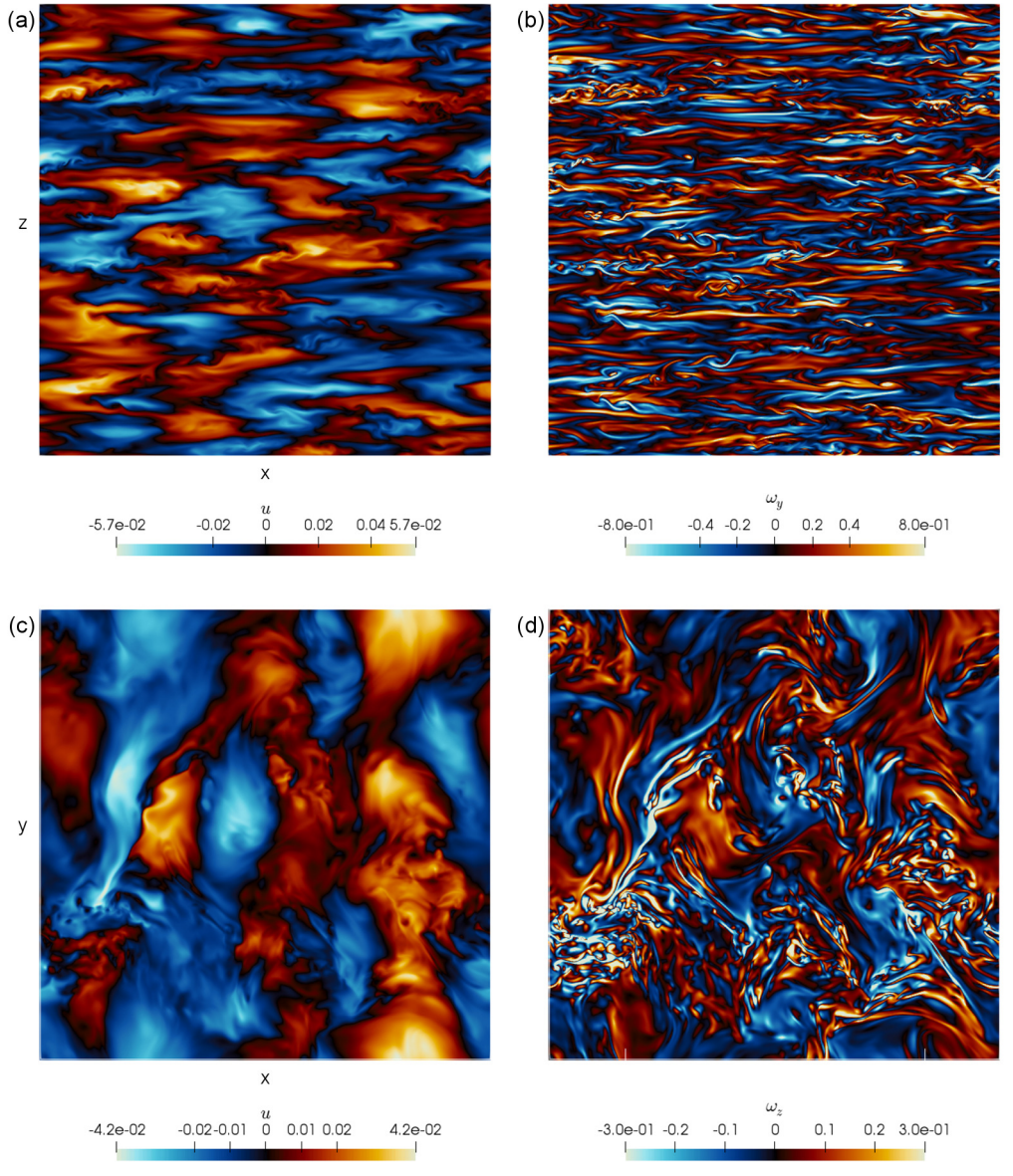

FIGURE 3. Top row: vertical slices (x, z) at $y = 0$ of (a) x-component velocity u and (b) y-component vorticity ω_y. Bottom row: horizontal slices (x, y) at $z = 0$ of (c) x-component velocity u and (d) z-component vorticity ω_z. All fields are computed at the end of run C1. Numerical values on the colourbars correspond to dimensional quantities.

small horizontal scales, since Re_b is not very large in this case. Dissipation at small wavenumbers disrupts the formation of a distinguishable true inertial subrange, which will be apparent in the spectral energy flux.

At k_b, $T_P(k_h)$ and $B(k_h)$ exhibit negative peaks coinciding with $T_K(k_h)$'s positive peak, but are much smaller in comparison. Overturning from the formation, instability, and breakdown of horizontal layers characteristically occurs at the buoyancy scale, so

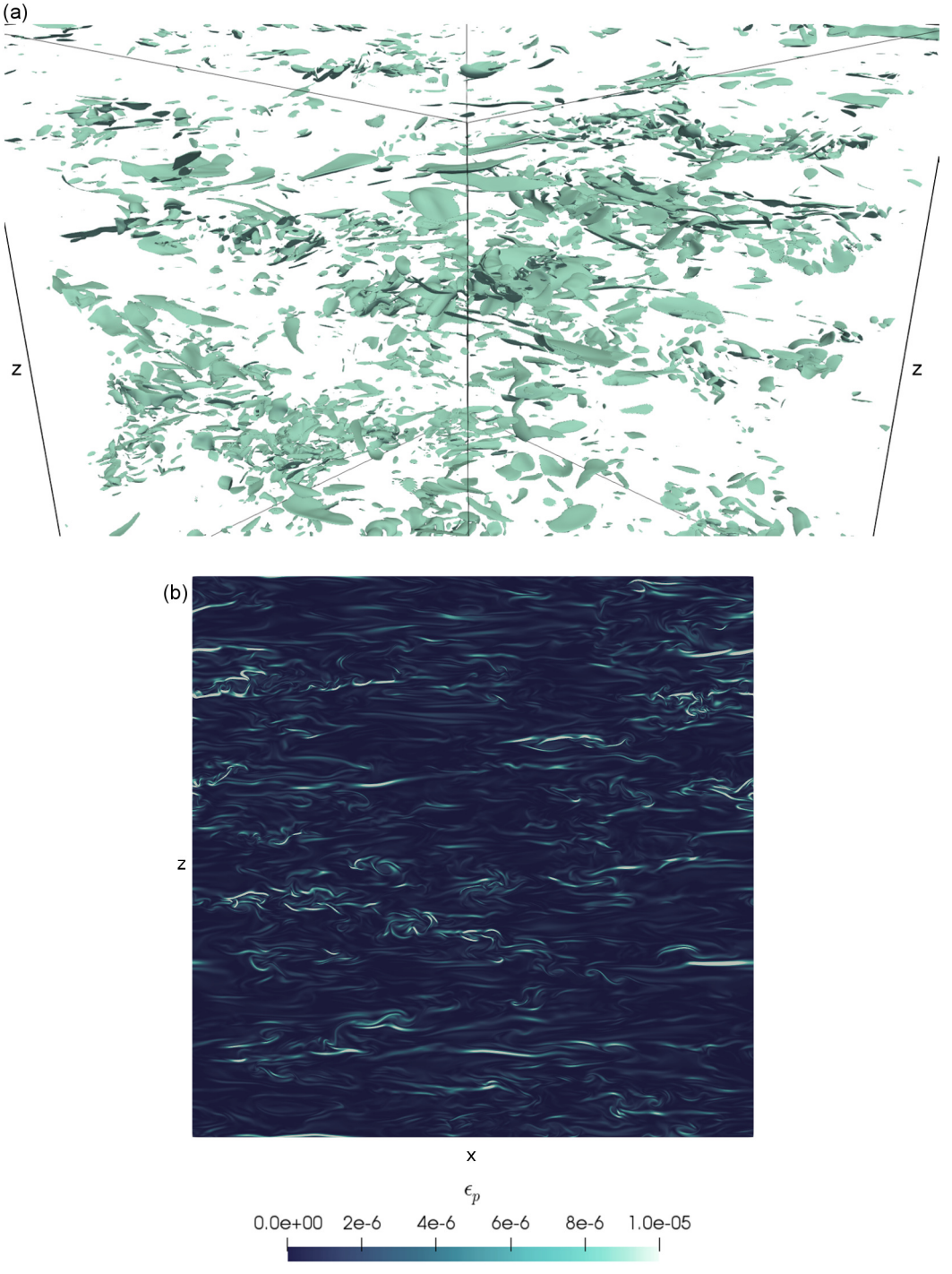

FIGURE 4. Potential energy dissipation field, ϵ_p, computed at the end of run C1: (a) isosurfaces of 5% of the maximum value, (b) vertical slice (x, z) at $y = 0$; numerical values on the colourbar correspond to dimensional quantities.

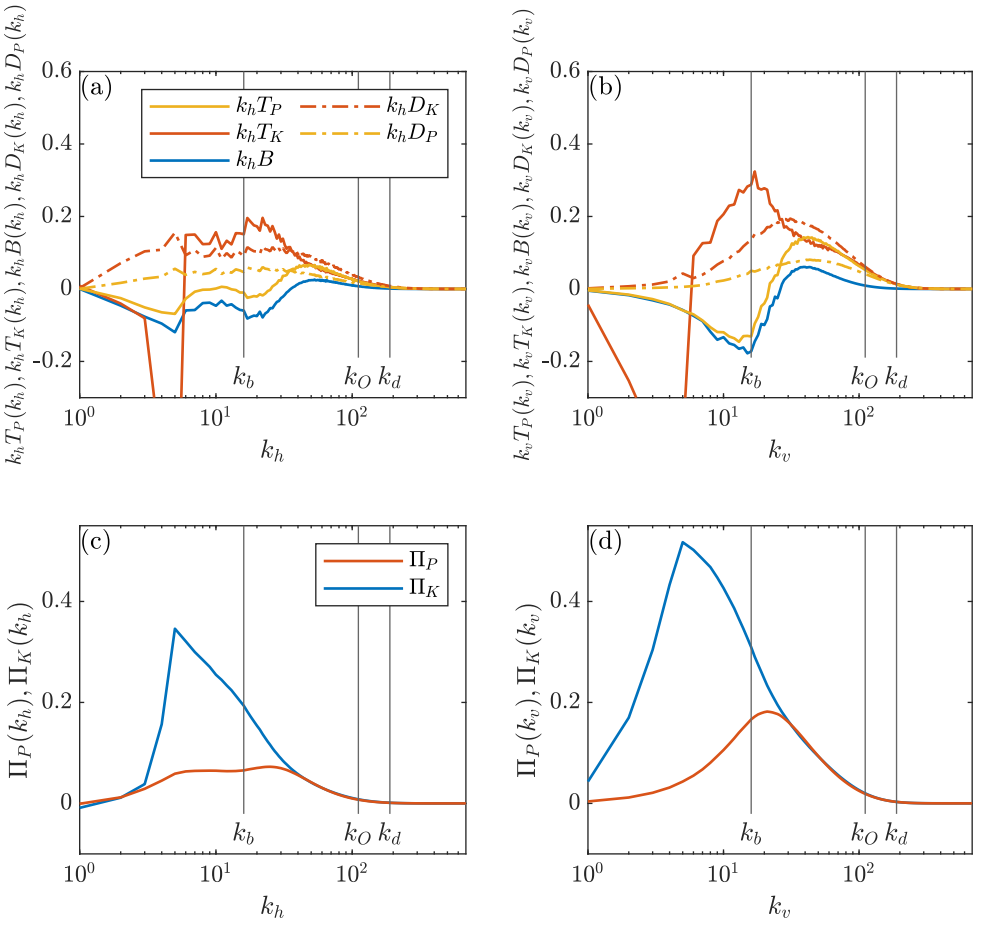

FIGURE 5. (a,b): Spectra for kinetic and potential energy transfer terms, kinetic and potential energy dissipation, and buoyancy flux for run C1. Spectra are multiplied by wavenumber to preserve area under the curve for linear-log axes. (c,d): Spectral energy fluxes for run C1.

some conversion of kinetic to potential energy is expected at k_b, as seen in Holloway (1988) and Waite (2011, 2014).

The vertical spectral budget shows different behaviour between the forcing interval and the buoyancy scale. At k_b, $T_K(k_v)$ has a prominent positive peak while $T_P(k_v)$ and $B(k_v)$ have negative peaks, and they are all comparable in magnitude indicating a smaller energy loss to dissipation than in the horizontal spectral budget. It is clear that in the vertical spectral budget, the overturning occurring at k_b is far more efficient at converting kinetic energy to potential energy than the horizontal.

Downscale of k_b and into the dissipation range, the horizontal and vertical spectral budgets behave similarly again. Between k_b and k_O, all of $T_P(k_h)$, $T_P(k_v)$, $B(k_h)$ and $B(k_v)$ increase to positive spectral peaks. At length scales below the buoyancy scale, buoyancy-driven processes dominate and large amounts of potential energy are expended to restratify the flow. Past k_O, viscous dissipation and buoyancy diffusion take over as the transfers and buoyancy flux decrease to zero.

The spectral energy fluxes Π_K and Π_P are shown in figure 5(c,d). While the fluxes are positive beyond the forcing scale, consistent with a downscale transfer of kinetic and potential energy, they do not exhibit discernable wavenumber ranges where downscale

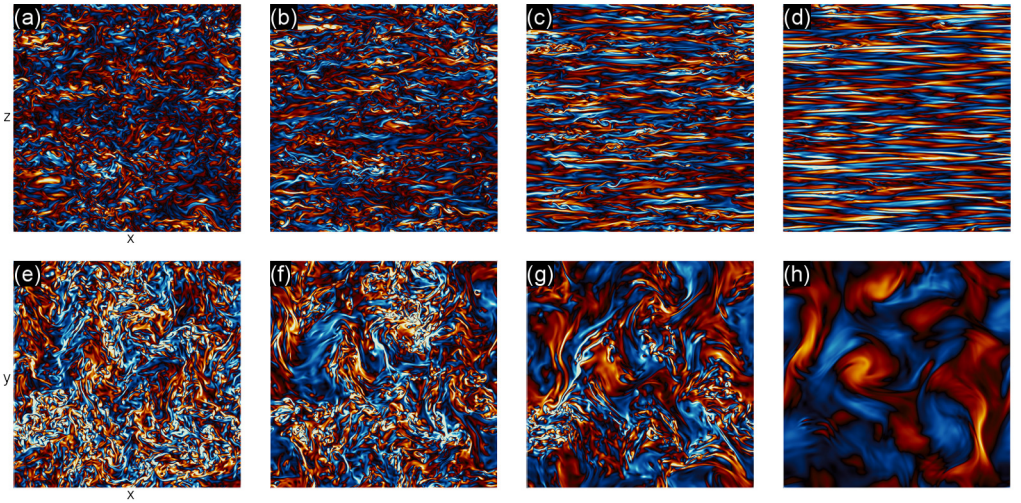

FIGURE 6. Top row: vertical slices (x, z) at $y = 0$ of y-component vorticity. Bottom row: horizontal slices (x, y) at $z = 0$ of z-component vorticity. $Pr = 1$ for (a,e) $Fr_f = 0.46$, (b,f) $Fr_f = 0.23$, (c,g) $Fr_f = 0.12$, and (d,h) $Fr_f = 0.058$. The same colourmap is used as in figure 3 with a modified range for visibility across Fr_f. The colourmap range shared by the vertical slices is different from the range shared by the horizontal slices.

energy flux is constant. However, since $T_P(k_h)$ is almost zero for a short wavenumber interval, there is more of a range of constant flux in potential than kinetic energy. The absence of a long inertial subrange is not unexpected, given the modest Re and Re_b of this case (Brethouwer *et al.* 2007). Beyond the forcing interval, $\Pi_K(k_h)$ and $\Pi_K(k_v)$ exhibit a large positive peak at larger wavenumbers. Dissipation at these large scales reduces the available energy for downscale transfer, inhibiting the development of a true inertial subrange.

The spectral fluxes for potential energy are smaller than the kinetic spectral fluxes at small horizontal and vertical wavenumbers, as the extreme negative spikes in $T_K(k_h)$ and $T_K(k_v)$ are directly caused by the large-scale forcing of kinetic energy. However, beyond the buoyancy scale, the kinetic and potential fluxes converge. The horizontal spectral fluxes in run C1 are small compared to the vertical spectral fluxes; this tends to depend on N, and will be further discussed in section 3.2.3.

3.1.2. *Fr_f-dependence for $Pr = 1$*

With fixed $Pr = 1$, decreasing Fr_f from 0.46 to 0.058 decreases Re_b from 28.7 to 0.567, and Fr_h from 0.0947 to 0.00935. Through the vertical slices in panels (a)-(d) of figures 6 and 7, we observe the transition in regimes from nearly isotropic small and intermediate scales to horizontally-layered flow in the vorticity and temperature fluctuation fields. Obvious layers are not visible in the vorticity field at the weakest stratification $Fr_f = 0.46$; the vertical temperature field slice in figure 7(a) better shows the slight anisotropy at $Re_b = 28.7$. At intermediate stratifications $Fr_f = 0.23$ and 0.12, KH instabilities are visible within recognizable horizontal layers in both the vorticity and temperature fields. Decreasing Fr_f reduces the thickness of these layers, corresponding to an increase in k_b. The turbulence becomes increasingly patchy with increasing stratification and the corresponding decrease in Re_b, with small-scale turbulence and overturning increasingly restricted to intermittent patches surrounded by viscously coupled layers (as in e.g. Brethouwer *et al.* 2007; Bartello & Tobias 2013;

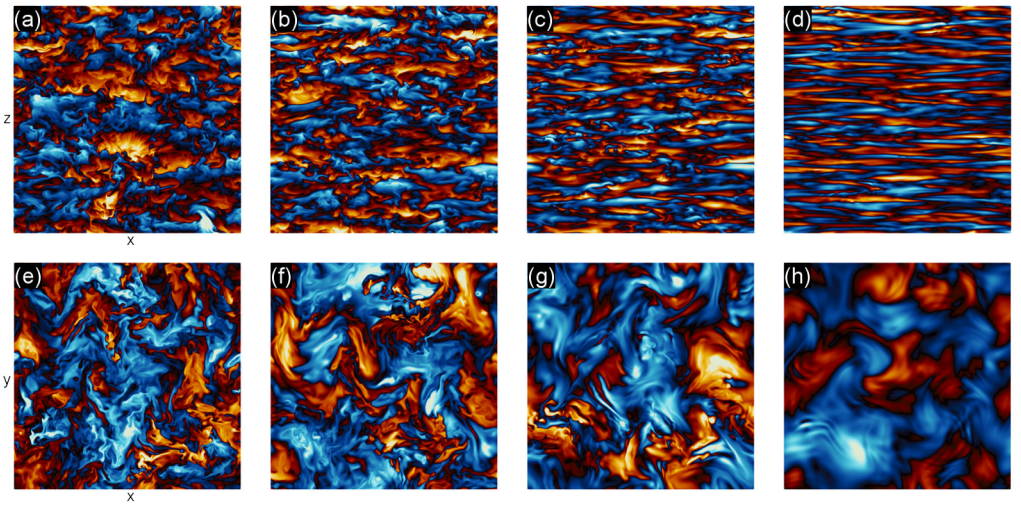

FIGURE 7. Top row: vertical slices (x, z) at $y = 0$ of θ. Bottom row: horizontal slices (x, y) at $z = 0$ of θ. $Pr = 1$ for (a,e) $Fr_f = 0.46$, (b,f) $Fr_f = 0.23$, (c,g) $Fr_f = 0.12$, and (d,h) $Fr_f = 0.058$. The colourmap range shared by the vertical slices is different from the range shared by the horizontal slices.

Waite 2014). For the strongest stratification $Fr_f = 0.058$, overturning is restricted to very small vertical scales and only a few instabilities are visible in figures 6,7(d).

The horizontal slices in panels (e)-(h) of figures 6 and 7 show the loss of small scale features, as the small scales become less turbulent with smaller Fr_f. This loss of small features can be attributed to k_O growing from 15 to 297 between $Fr_f = 0.46$ and 0.058 while k_d is only slightly increased. At larger Fr_f, the flow resembles small scale isotropic turbulence for a wider wavenumber range $k \in [k_O, k_d]$, so the loss of small-scale features at $Fr_f = 0.058$ is in line with greater anisotropy. At $Fr_f = 0.058$, signatures of KH billows are still visible in the horizontal slices (figures 6,7(h)). These panels also exhibit the least extreme values in temperature and vorticity: as the horizontal layers are reduced to vertical scales near k_d (and k_B in the case of $Pr = 1$), fluctuations in these fields are eliminated by viscous dissipation and buoyancy diffusivity.

The compensated kinetic and potential energy spectra for $Pr = 1$ at each Fr_f are plotted in figure 8 in terms of horizontal and vertical wavenumber. For the horizontal kinetic energy spectra in figure 8(a), the $Fr_f = 0.46$, 0.23, and 0.12 cases are very similar. Slightly more kinetic energy is found at large scales for smaller Fr_f, and these cases show agreement with the $k_h^{-5/3}$ scaling law for almost a decade after the forcing interval. The vertical kinetic energy spectra in figure 8(b) are also affected by Fr_f. As k_b increases with decreasing Fr_f, the compensated spectra approximately exhibit the +3 slope (as in section 3.1.1) for a longer range of small wavenumbers, but eventually converge at $k_v \approx 100$. A short plateau region corresponding to limited agreement with k_v^{-3} scaling is observed at the three lowest stratifications.

The horizontal potential energy spectra for $Fr_f = 0.46$, 0.23, and 0.12 follow the same patterns as the kinetic energy, but with marginally more Fr_f-dependence at intermediate and large k_h. Downscale of k_b, the spectra steepen more for smaller Fr_f but eventually converge far into the dissipation range. More potential energy is found at intermediate to large k_h at weaker stratification which is consistent with more small scale overturning in the temperature field. The compensated vertical potential energy spectra nearly have

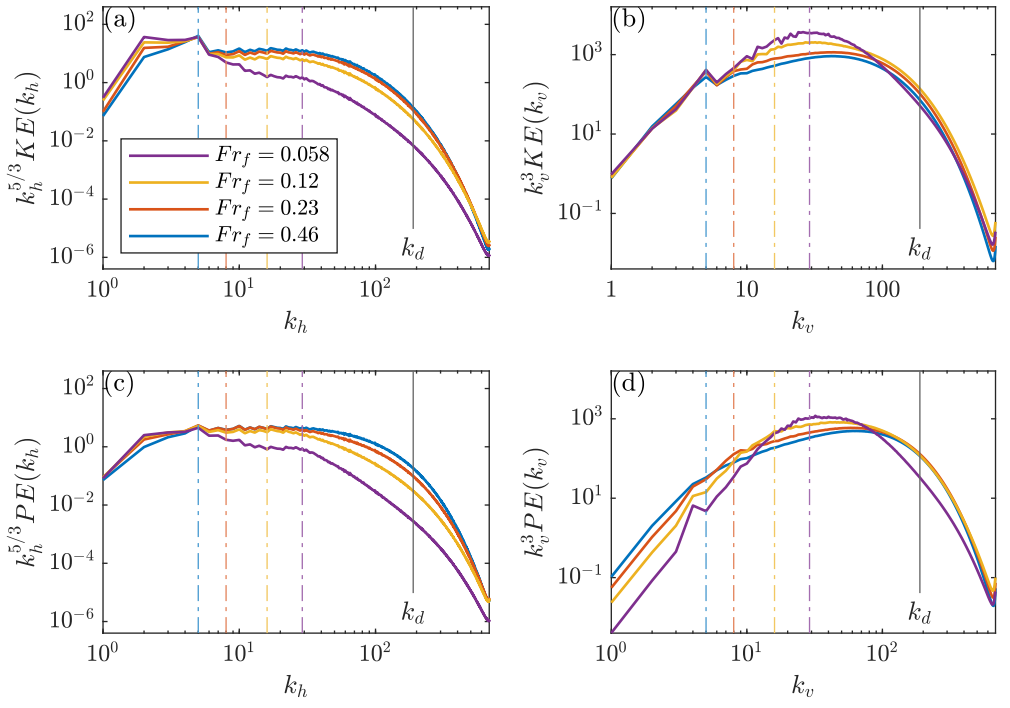

FIGURE 8. Energy spectra in terms of horizontal and vertical wavenumbers for $Pr = 1$ at different Fr_f. Vertical dash-dotted lines are buoyancy scales corresponding to Fr_f colours. The average k_d and k_B are the same for $Pr = 1$.

the +3 slope up until their respective k_b, and exhibit similar dependence on Fr_f as in the vertical kinetic energy spectra.

In all panels, the $Fr_f = 0.058$ spectra have a distinct shape compared to the three weaker stratifications. Since $Re_b = 0.6 < 1$, in this case, the cascade to small horizontal scales is suppressed and there is a consequent steepening of the horizontal spectra (e.g. Brethouwer *et al.* 2007; Waite 2014). The steepening of the $Fr_f = 0.058$ horizontal spectra at small wavenumbers is severe enough that there is little $k_h^{-5/3}$ scaling law agreement just downscale of the forcing. Similarly, the steepening from k_b onwards causes the $Fr_f = 0.058$ vertical spectra to deviate from k_v^{-3} scaling. Except in figure 8(b), the $Fr_f = 0.058$ case does not converge to the other three cases until the end of the wavenumber range. Strong stratification will restrict vertical advection, which greatly reduces the potential energy found at small vertical length scales.

3.2. *Pr-dependence*

3.2.1. *Energy spectra*

We now examine the effects of varying Pr in fixed-Fr_f groups, starting with the kinetic and potential energy spectra. The effect of Pr on the horizontal and vertical kinetic energy spectra, shown in figure 9, is more obvious and extends to larger scales, as Fr_f and Re_b decrease. Specifically, while Pr-dependence for $Fr_f = 0.46$ and 0.23 are mostly downscale of k_O and around k_d (figures 9(a-d)), the $Fr_h = 0.12$ and 0.058 cases show Pr-dependence that extends upscale past k_O and into intermediate scales (figures 9(e-h)). Otherwise, as in figure 2, spikes at small wavenumbers are from the large-scale forcing, and the vertical spectra roughly have a +3 slope until k_b regardless

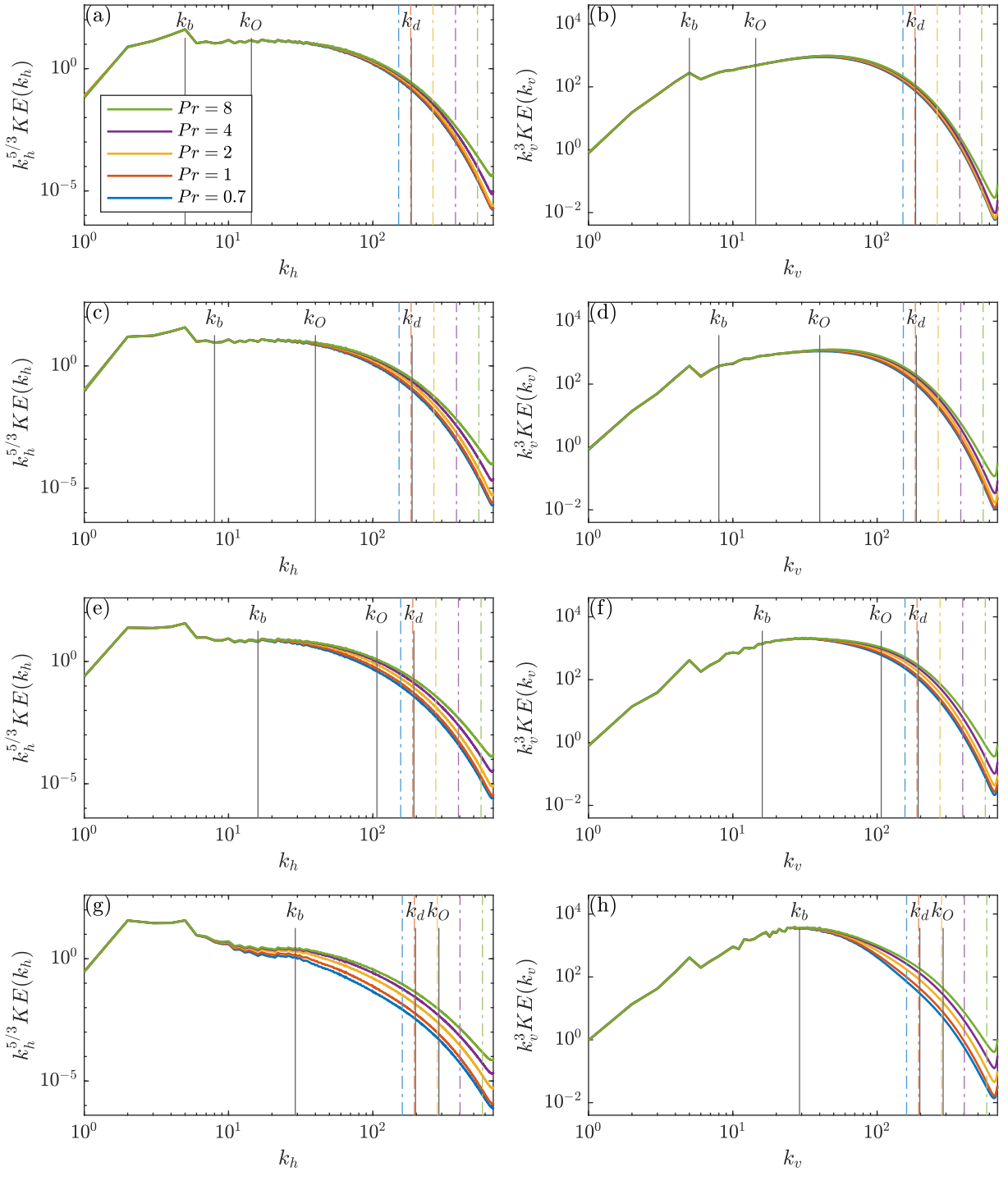

FIGURE 9. Compensated kinetic energy spectra in terms of horizontal and vertical wavenumbers for different Pr. From top to bottom the rows are $Fr_f = 0.46, 0.23, 0.12, 0.058$. Vertical dash-dotted lines are k_B corresponding to Pr colours.

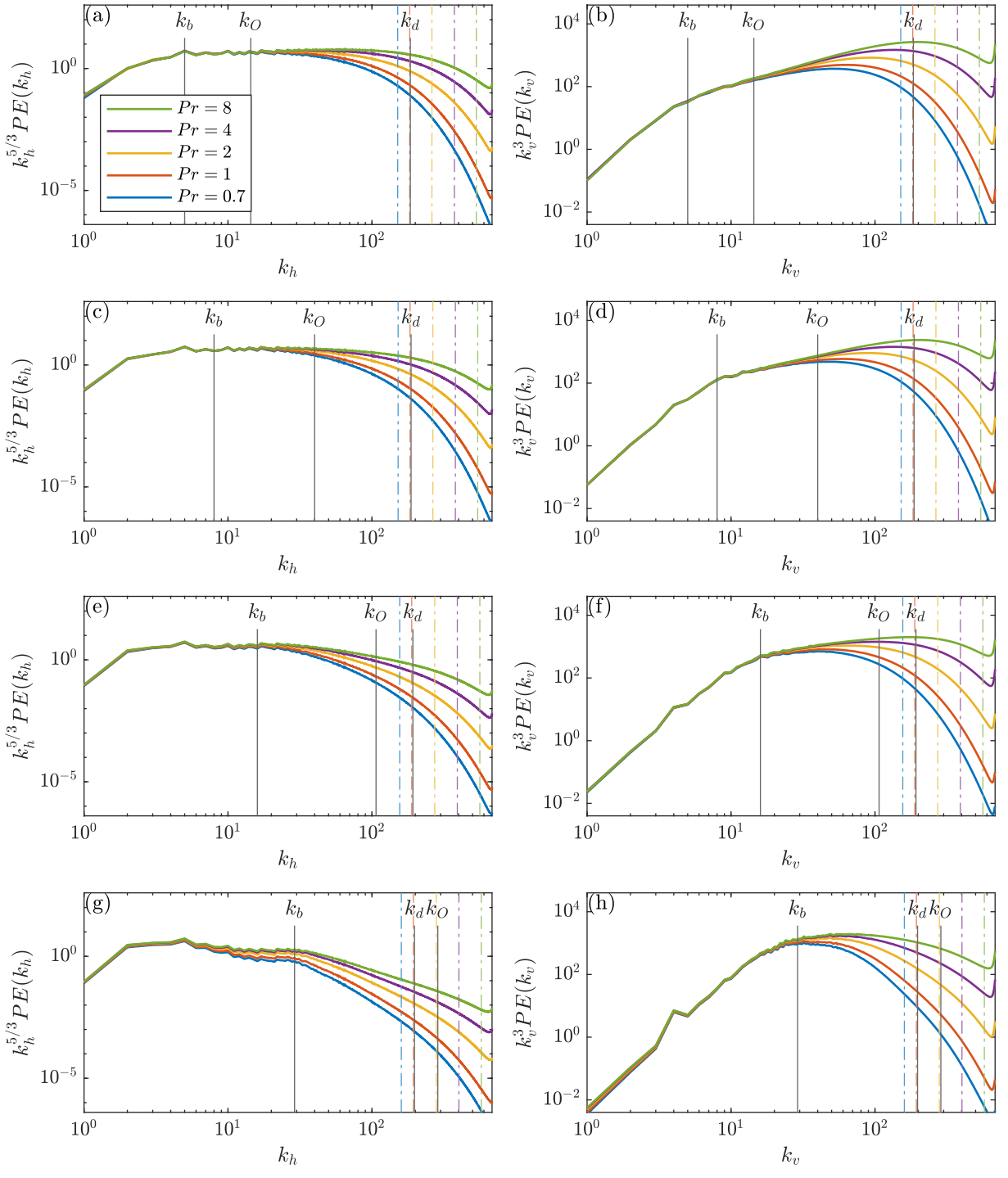

FIGURE 10. Compensated potential energy spectra in terms of horizontal and vertical wavenumbers for different Pr. From top to bottom the rows are $Fr_f = 0.46, 0.23, 0.12, 0.058$. Vertical dash-dotted lines are k_B corresponding to Pr colours.

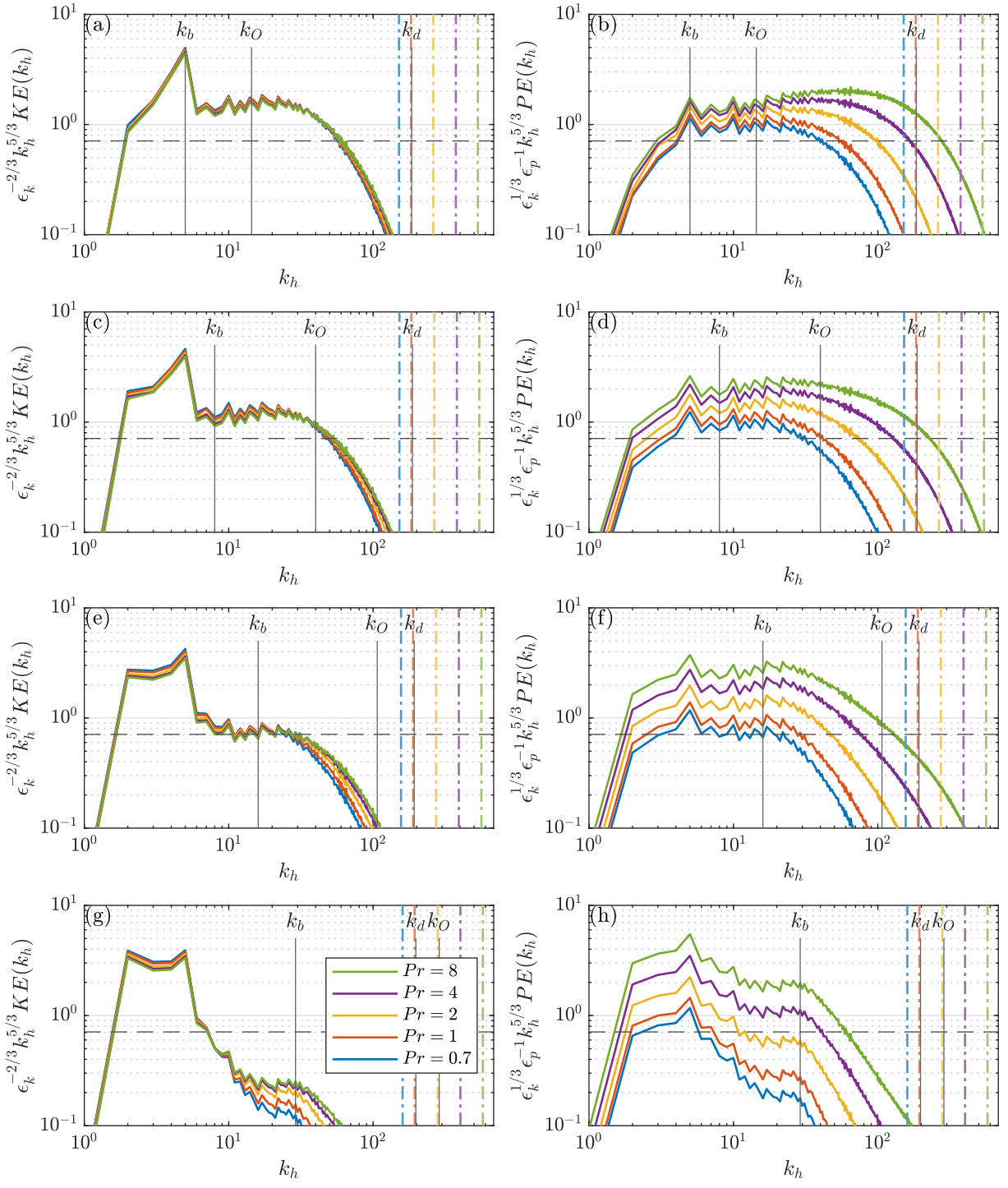

FIGURE 11. Compensated horizontal wavenumber spectra for dimensional kinetic energy (left column) and potential energy (right column). From top to bottom the rows are $Fr_f = 0.46$, 0.23, 0.12, and 0.058. Vertical dash-dotted lines are k_B corresponding to Pr colours. Horizontal lines are reference Kolmogorov and Obukhov-Corrsin constants of the two-dimensional horizontal spectra: $C_1' = C_2' = 0.71$ (Lindborg 2006; Brethouwer *et al.* 2007).

Run	Fr_f	Pr	$KE(k_h)$	$KE(k_v)$	$PE(k_h)$	$PE(k_v)$
A0	0.46	0.7	-2.04	-2.43	-1.98	-2.21
A1	0.46	1	-2.01	-2.41	-1.84	-2.07
A2	0.46	2	-1.97	-2.39	-1.67	-1.90
A3	0.46	4	-1.95	-2.36	-1.55	-1.77
A4	0.46	8	-1.93	-2.35	-1.47	-1.69
B0	0.23	0.7	-2.09	-2.79	-2.20	-2.59
B1	0.23	1	-2.04	-2.76	-2.07	-2.43
B2	0.23	2	-1.96	-2.70	-1.87	-2.20
B3	0.23	4	-1.92	-2.66	-1.75	-2.07
B4	0.23	8	-1.89	-2.64	-1.67	-1.98
C0	0.12	0.7	-2.35	-4.07	-2.51	-3.91
C1	0.12	1	-2.26	-3.97	-2.35	-3.53
C2	0.12	2	-2.13	-3.82	-2.13	-3.00
C3	0.12	4	-2.05	-3.70	-1.98	-2.67
C4	0.12	8	-2.00	-3.62	-1.89	-2.47
D0	0.058	0.7	-2.92	-5.85	-2.46	-5.86
D1	0.058	1	-2.76	-5.63	-2.31	-5.26
D2	0.058	2	-2.55	-5.26	-2.13	-4.33
D3	0.058	4	-2.43	-4.97	-2.02	-3.69
D4	0.058	8	-2.38	-4.77	-1.96	-3.27

TABLE 2. Slopes from linear regression analysis of kinetic and potential energy spectra in figures 9 and 10. For horizontal spectra, the linear regression is performed over $k_h \in [6, 60]$ except for $Fr_f = 0.058$, where $k_h \in [6, 29]$ is used. For vertical spectra, the wavenumber interval is one decade starting at k_b; i.e. $k_v \in [6, 60], [8, 80], [16, 160]$ for $Fr_f = 0.46, 0.23, 0.12$ respectively. The vertical spectra for $Fr_f = 0.058$ uses $k_v \in [29, 200]$ since the average $k_d \approx 198$.

of Fr_f and Re_b. For $Fr_f = 0.46$, 0.23, and 0.12, the horizontal spectra follow the $k_h^{-5/3}$ scaling law just after the forcing interval for about one decade as in run C1 (see table 2). The $Fr_f = 0.058$ spectra are steeper than those at larger Fr_f, with a more pronounced bump at k_b (Waite 2014). Similarly, in the vertical wavenumber spectra, a short plateau corresponding to the k_v^{-3} scaling law is observed for almost one decade for all groups except $Fr_f = 0.058$. Beyond these short scaling law intervals, both the horizontal and vertical spectra shallow slightly when Pr is increased (table 2). Larger-Pr simulations contain more kinetic energy at small scales since buoyancy-induced velocity fluctuations can persist as k_B increases. As a result of the spectra shallowing, the $k_h^{-5/3}$ and k_v^{-3} scaling laws extend to slightly smaller scales.

As stratification increases, the dependence on Pr extends to smaller wavenumbers. For example, the compensated horizontal kinetic energy spectra for different Pr start to diverge at $k_h \approx 30$ (between the Ozmidov and Kolmogorov wavenumbers) for $Fr_f = 0.46$ and $k_h \approx 20$ (well upscale of the Ozmidov scale) for $Fr_f = 0.12$ in figures 9(a) and 9(e) respectively. Only for the horizontal spectra with $Fr_f = 0.058$ and $Re_b < 1$ (figure 9(g)) do the spectra for each Pr separate shortly after the forcing interval, and at a wavenumber smaller than k_b.

The potential energy spectra in figure 10 show similar but more pronounced changes as Pr is varied. Both horizontal and vertical spectra exhibit the same shallowing with increased Pr at large wavenumbers as in the kinetic energy spectra (table 2). In the horizontal spectra, the shallowing that results from increasing Pr again lengthens the

wavenumber range for which there is agreement with $k_h^{-5/3}$ scaling. Decreasing Fr_f increases the average k_b, where a break in the vertical spectra is observed: immediately after k_b, the spectral slopes decrease toward a k_v^{-3} scaling region. In the vertical spectra for $Fr_f = 0.46$, 0.23, and 0.12, the shallowing from larger Pr causes the spectra to become shallower than the k_v^{-3} scaling law downscale of k_b.

The $Fr_f = 0.058$ potential energy spectra (figure 10(g,h)) behave similarly to the kinetic energy spectra at this stratification: here, both the horizontal and vertical spectra visibly separate just after the forcing interval and before k_b. The separation occurs at a noticeably smaller wavenumber for the horizontal spectra than the vertical, as in the kinetic energy case. All simulations with $Fr_f = 0.058$ have $Re_b < 1$; horizontal scales between the forcing interval and the buoyancy scale are sensitive to Pr because of diffusive effects between the layers of quasi-horizontal vortices. Figure 10(g) for $Fr_f = 0.058$ also shows a break in the horizontal spectra at k_b, after which each curve steepens beyond $k_h^{-5/3}$.

The Kolmogorov and Obukhov-Corrsin constants from (1.15)-(1.16) can be determined for each simulation from the fully compensated energy spectra, $\epsilon_k^{-2/3} k_h^{5/3} E_K(k_h)$ and $\epsilon_k^{1/3} \epsilon_p^{-1} k_h^{5/3} E_P(k_h)$ (figure 11). Since the simulations in this work use the two-dimensional horizontal wavenumber k_h, the converted $C' \approx 1.40C$ values will be discussed. The compensated spectra generally show C_1' and C_2' to be larger than the value $C' = 0.71$, corresponding to $C = 0.51$ referenced in Lindborg (2006); Brethouwer *et al.* (2007). The kinetic energy spectra in the left column show C_1' to be insensitive to Pr when $Re_b > 1$. However, as Re_b increases and stratification decreases, the value of C_1' tends to increase, which is consistent with the results of Brethouwer *et al.* (2007); Bartello & Tobias (2013) (compared to figure 12 and figure 9a therein, respectively). Further, the present simulations with $Re_b \approx 8$ (figure 11c) show C_1' slightly larger than 0.71, similar to comparable simulations in Brethouwer *et al.* (2007) (figure 13a therein, $Re_b \approx 9$) and Bartello & Tobias (2013) (figure 9a therein, cyan curve, $Re_b \approx 10$). The compensated potential energy spectra show C_2' to be increasingly dependent on Pr as stratification increases and Re_b decreases. This may be attributed to the Pr-dependence of the mixing efficiency: across all simulations, the sum $\epsilon_k + \epsilon_p$ is nearly held fixed, while the ratio ϵ_p/ϵ_k decreases with larger Pr. The potential energy spectra compensated with wavenumber only (figure 10, left column) are much less dependent on Pr when $Re_b > 1$. The larger-Pr simulations simultaneously exhibit increasing ϵ_k and decreasing ϵ_p, thereby resulting in C_2' being strongly dependent on Pr through the premultiplication factor $\epsilon_k^{1/3} \epsilon_p^{-1}$.

For each increase in Pr, there appears to be less of a change in the shape of the spectra, and this behaviour is observed at all Fr_f. Excluding $Pr = 0.7$, each jump in Pr is from doubling the previous Pr, but the shallowing or separation between successive curves slightly decreases, as evident in Table 2. This is especially true at scales around and above the Kolmogorov scale. For instance, at the average $k_d = 193$ for $Fr_f = 0.12$, between $Pr = 1$ and $Pr = 2$ the horizontal kinetic energy increases by 67% compared to a 38% increase from $Pr = 4$ to $Pr = 8$. The vertical potential energy for the same Fr_f and k_d increases by 310% between $Pr = 1$ and $Pr = 2$ compared to a 76% increase from $Pr = 4$ to $Pr = 8$. Simulations where Pr is much greater than 8 may be expected to continue exhibiting less of a change in the potential energy spectra shape as Pr is increased. That is, the diminishing increase and shallowing of spectra at larger Pr may become so inappreciable that these higher-Pr spectra converge to a shape not vastly different from the $Pr = 8$ case, at least at wavenumbers at and below k_d. At larger wavenumbers, for very large $Pr \sim O(10^3)$, buoyant scalars have been shown to behave as

passive scalars (i.e. potential energy spectra proportional to k^{-1}), and plateaus ($\propto k^0$) eventually develop in the potential energy spectra (Okino & Hanazaki 2017, 2019, 2020).

3.2.2. *Buoyancy flux*

Buoyancy flux spectra are shown in figure 12 at different Pr in fixed-Fr_f groups as in section 3.2.1 for the energy spectra. Overall, an increase in buoyancy flux is observed in all cases as Pr is increased. The increase in buoyancy flux is most significant at large horizontal and vertical wavenumbers, where restratification occurs, and is amplified at smaller Fr_f. This increase in small-scale buoyancy flux with increasing Pr is consistent with the monotonic decrease in ϵ_p/ϵ_k, shown in table 1 and found in previous DNS studies of stratified turbulence (Smyth *et al.* 2001; Stretch *et al.* 2010; Salehipour *et al.* 2015); while the overall buoyancy flux is negative, an increase in small scale buoyancy flux means that some small-scale potential energy is converted back to, and dissipated as, kinetic energy. The one exception to this trend is for the strongest stratification and smallest Re_b (figure 12(g)), where the increased buoyancy flux is greatest at small horizontal and large vertical wavenumbers. Additionally, at $Fr_f = 0.058$, the horizontal buoyancy flux is positive for a short wavenumber range before k_b, as well as at larger wavenumbers, for $Pr = 2$, 4, and 8. It makes sense that a greater amount of potential energy is converted to kinetic energy as Pr is increased: there is more potential energy available at large wavenumbers for either nonlinear transfer or conversion to kinetic energy when buoyancy diffusivity is weakened (figure 10). Restratification is less suppressed for less intense turbulence (Holloway 1988); indeed, for these simulations, increasing Pr at a fixed Fr_f is associated with a decrease in Re.

The right column of figure 12 shows restratification to consistently take place at small vertical scales downscale of k_b. Due to the tendency towards isotropy at small scales, this positive spectral bump is also observed in the horizontal buoyancy flux spectra at a comparable k_h range, at least for $Fr_f = 0.46$, 0.23, and 0.12. The $Fr_f = 0.058$ case is different. All these simulations have $Re_b < 1$; as a result, there is no small-scale isotropy, and these small vertical scales are associated with large horizontal scales by viscously coupled layers. In this regime of stratified turbulence, it is reasonable that the buoyancy flux at large horizontal scales is heavily affected by Pr, since buoyancy diffusion at small vertical scales can characteristically occur between these layers. Figure 12(g) also reveals that the Pr-dependence of buoyancy flux is sensitive enough at large horizontal scales to even influence the direction of kinetic-to-potential energy conversion. Buoyancy diffusion can become weak enough at a sufficiently large Pr so that at large horizontal scales, enough surplus potential energy may be made available for a positive buoyancy flux.

The dependence on Pr seems to be decreasing with increasing Pr, as seen in the energy spectra. For example, the separation between the buoyancy flux spectra in the $Pr = 4$ and $Pr = 8$ cases is noticeably smaller than for preceding Pr increments. This suggests convergence of the buoyancy flux spectra at large Pr (even moreso than for the energy spectra).

3.2.3. *Spectral flux*

The spectral energy fluxes Π_K and Π_P are shown in figures 13 and 14, respectively. The spectral flux for kinetic energy is not significantly affected by varying Pr, especially for the vertical wavenumber spectra (figure 13, right column). For the intermediate stratifications $Fr_f = 0.23$ and 0.12, while there is a slight increase in flux with increasing Pr, the fluxes at each Pr are scarcely distinguishable between the forcing interval and dissipation range in both horizontal and vertical spectra.

The $Fr_f = 0.058$ case is different, and shows a greater dependence of $\Pi_K(k_h)$ and

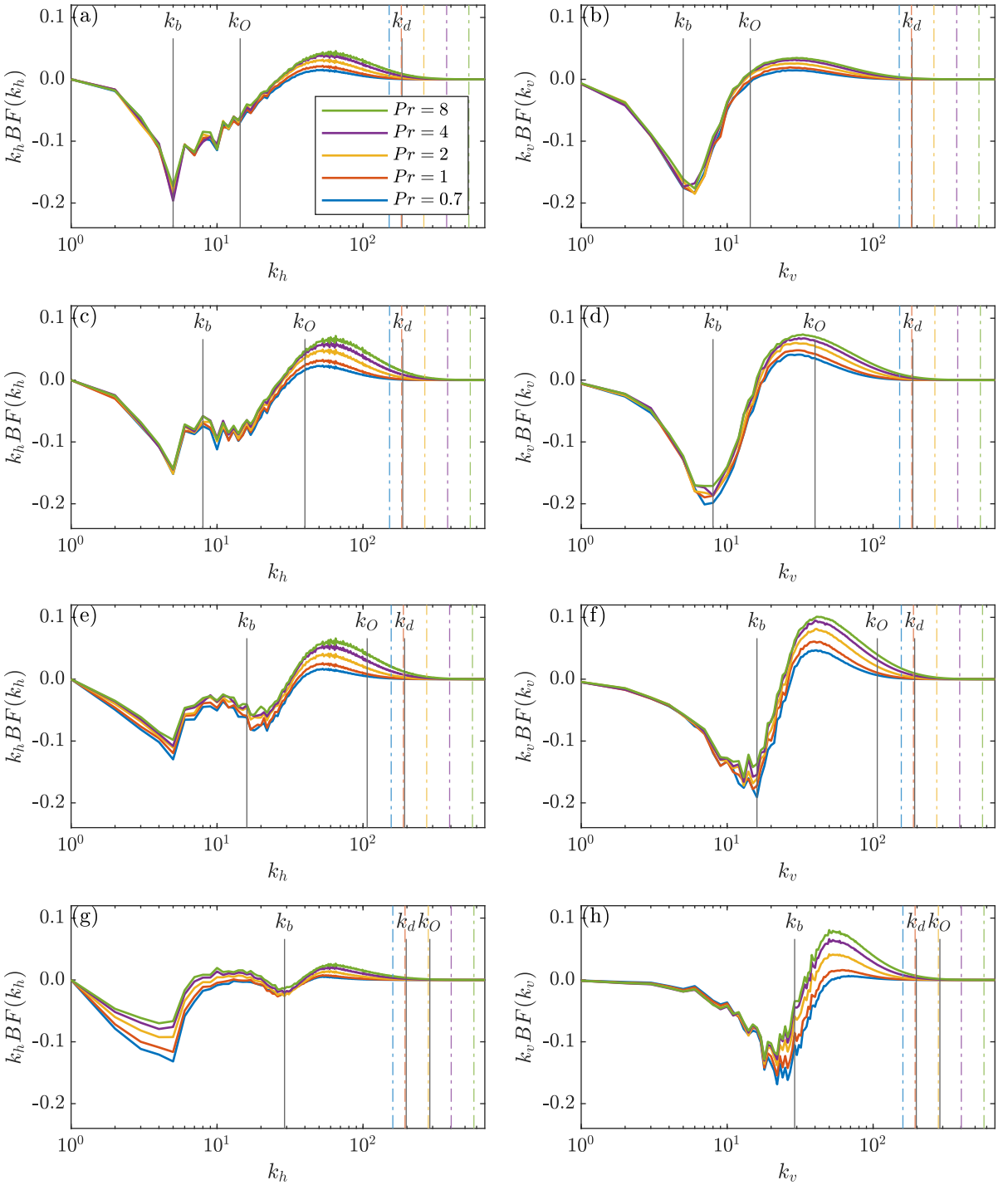

FIGURE 12. Buoyancy flux spectra multiplied by wavenumber to preserve area under the curve for linear-log axes. From top to bottom the rows are $Fr_f = 0.46$, 0.23, 0.12, and 0.058. Horizontal (left) and vertical (right) wavenumber spectra are shown. Vertical dash-dotted lines are k_B corresponding to Pr colours.

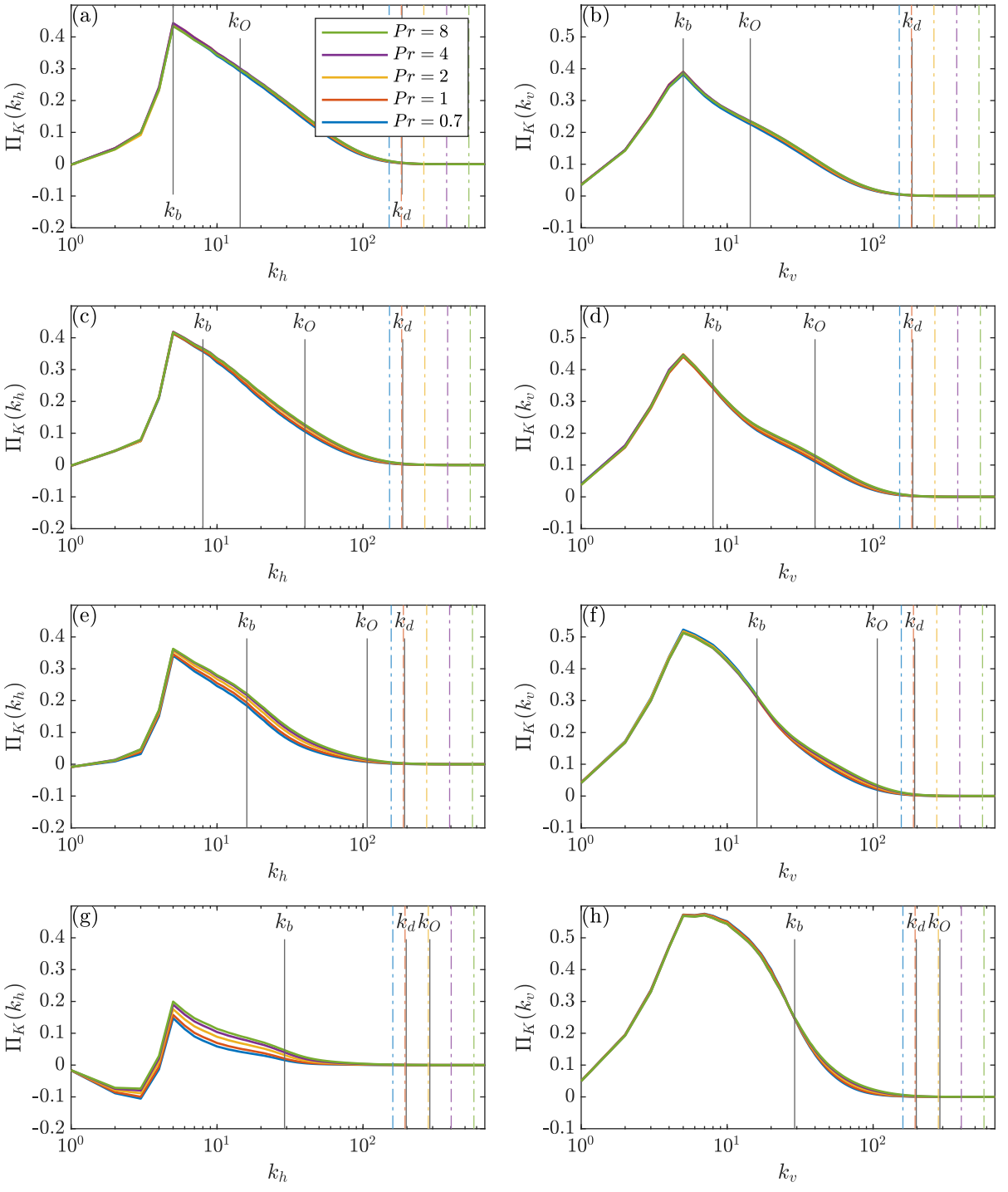

FIGURE 13. Spectral kinetic energy flux, as in equation (2.12). From top to bottom the rows are $Fr_f = 0.46$, 0.23, 0.12, and 0.058. Horizontal (left) and vertical (right) wavenumber spectra are shown. Vertical dash-dotted lines are k_B corresponding to Pr colours.

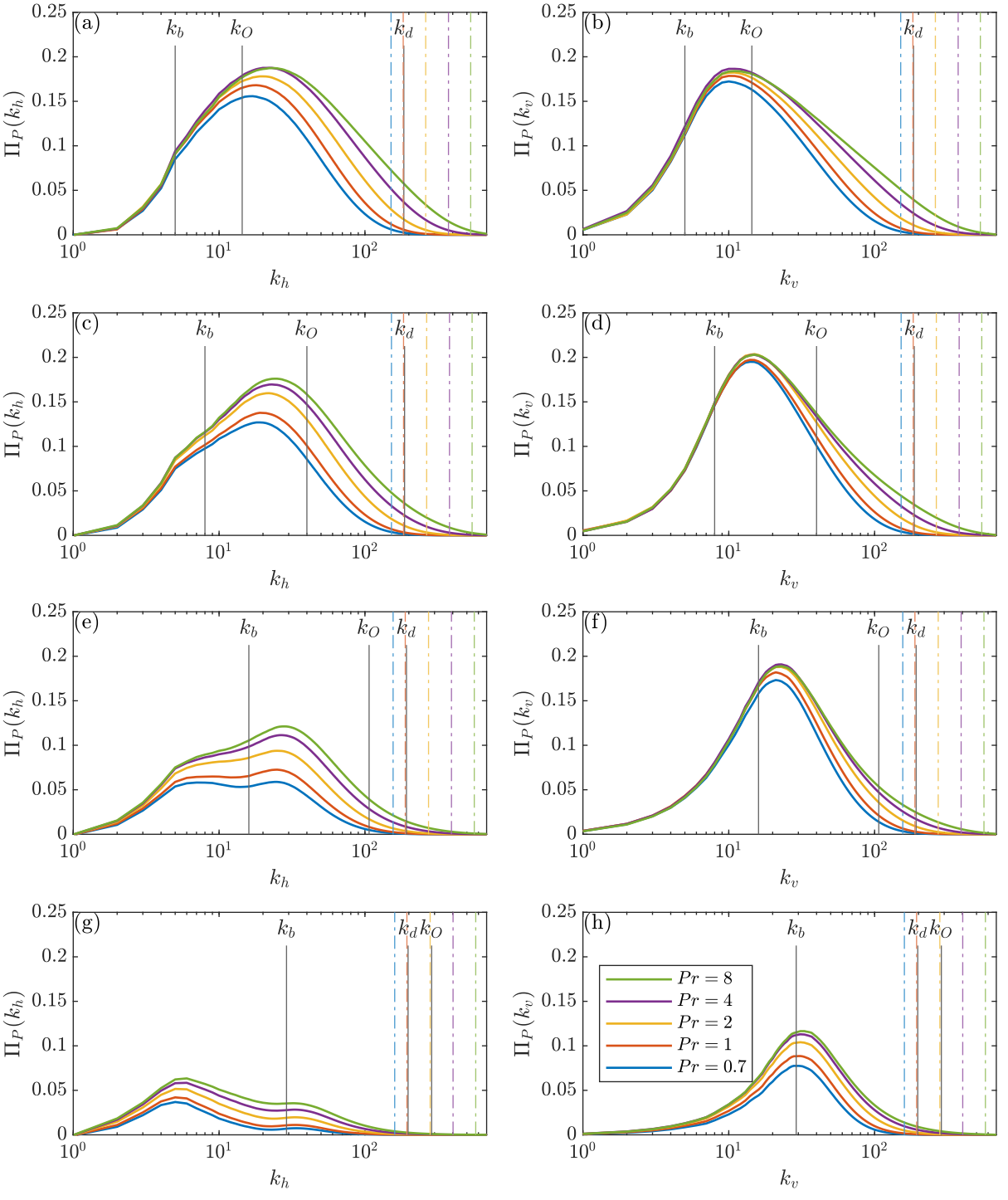

FIGURE 14. Spectral potential energy flux, as in equation (2.13). From top to bottom the rows are $Fr_f = 0.46$, 0.23, 0.12, and 0.058. Horizontal (left) and vertical (right) wavenumber spectra are shown. Vertical dash-dotted lines are k_B corresponding to Pr colours.

$\Pi_K(k_v)$ on Pr. The horizontal flux $\Pi_K(k_h)$ changes with Pr at large horizontal scales (figure 13), and is the only case where the fluxes are negative for a short wavenumber range. At very small horizontal wavenumbers, upscale transfer and accumulation of energy at large scales would appear as positive $T_K(k_h)$ at small k_h, corresponding to the energy contained in vertically sheared horizontal layers when $Re_b < 1$. Downscale of the forcing interval, the Pr-dependence of $\Pi_K(k_h)$, while more apparent than at lower stratifications, is still minor. From the buoyancy flux in figure 12(g), less kinetic energy is lost by conversion to potential energy at greater Pr, slightly increasing the available kinetic energy for downscale transfer. The vertical flux $\Pi_K(k_v)$ for $Fr_f = 0.058$ is the closest to displaying a (short) constant flux range. Otherwise, varying Pr has little effect on $\Pi_K(k_v)$.

The impact of Pr on the potential energy spectral flux is more pronounced than for the kinetic flux (figure 14). In all cases, increasing Pr increases the potential energy spectral flux. From figure 10, an increase in potential energy is found with larger Pr, but for a limited wavenumber range. In the horizontal flux $\Pi_P(k_h)$ for cases $Fr_f = 0.46$, 0.23, and 0.12, the most significant change is at intermediate-to-high wavenumbers, but the large horizontal scales are still minimally affected. The $Fr_f = 0.46$ case shows Pr-dependence only for $k_h > k_b$, but for more strongly stratified cases, the Pr-dependence extends up to the forcing interval. The termination of forward potential energy flux adjusts with Pr as expected, and more potential energy is made accessible for downscale transfer at large horizontal scales, since buoyancy diffusion acts on a shorter range of associated vertical scales.

The vertical spectral fluxes are almost unaffected by Pr upscale of k_b in all but the most strongly stratified case. This is to be expected of stratified turbulence, as the buoyancy scale characterizes the horizontal layer thickness and largest vertical overturning scale; the processes responsible for potential energy transfer should be limited by k_b.

Both the horizontal and vertical potential energy fluxes are far smaller for $Fr_f = 0.058$ than the three weaker stratifications. Notably, for $Fr_f = 0.58$, the influence of Pr on the horizontal and vertical spectra persist for almost the entire wavenumber range. In the vertical flux, Pr-dependence of the potential energy flux even occurs at vertical scales larger than the layer thickness as the flow becomes more anisotropic with $Re_b < 1$. A change in Π_P would be expected when buoyancy diffusivity is weakened, but the influence of Pr extends upscale past the dissipation range in figure 14. The potential energy spectral fluxes are closer to exhibiting ranges of constant flux than for kinetic energy, but Re may still be too small for a discernable inertial range.

Again, as in the buoyancy flux spectra and energy spectra, the difference in both spectral energy fluxes between $Pr = 4$ and $Pr = 8$ is noticeably smaller than the preceding increases of Pr. As Pr increases, Π_K and Π_K may also be expected to converge to limiting curves.

3.2.4. *Physical space fields*

Lastly, slices of physical space fields are examined for fixed $Fr_f = 0.12$ as Pr is increased ($Pr = 0.7$ is excluded as it is similar to the $Pr = 1$ case). Since they have fixed Fr_f, these runs have a similar $Re_b \approx 2$; the only noticeable change in the velocity, vorticity, and temperature fluctuation fields is that smaller scale features emerge as Pr increases. The changes are subtle, but close inspection of the θ field slices in figure 15 reveal the finer structures that are able to persist with larger Pr. The patchiness of the turbulence, which varies strongly with Re_b, does not seem to depend much on Pr. This trend is also observed in the velocity and vorticity fields, so only the temperature and the potential energy dissipation field are shown in figures 15 and 16.

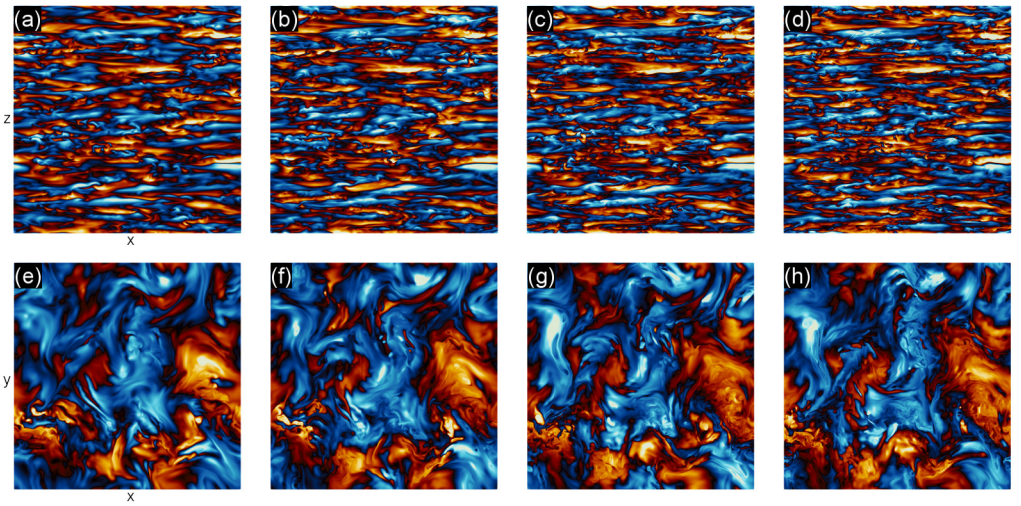

FIGURE 15. Top row: vertical slices (x, z) at $y = 0$ of θ. Bottom row: horizontal slices (x, y) at $z = 0$ of θ. Fixed $Fr_f = 0.12$ for (a,e) $Pr = 1$, (b,f) $Pr = 2$, (c,g) $Pr = 4$, and (d,h) $Pr = 8$. The same colourmap is used as in figure 3 with the range modified for visibility across Pr. The colourmap range shared by the vertical slices is different from the range shared by the horizontal slices.

Vertical slices of the potential energy dissipation field are plotted in figure 16 for $Pr = 1$, 2, 4, and 8. The dissipative regions follow the horizontal layers, including the small-scale overturning and instabilities. At smaller Pr, a bigger portion of the domain is dissipative, since a wider range of small scales is accessible to the stronger buoyancy diffusivity. The dissipative regions at $Pr = 8$ are limited to extremely fine scales, which is in agreement with the largest k_B for $Fr_f = 0.12$. Larger-Pr simulations are expected to exhibit even smaller scale details in their physical fields, but may require higher resolution than $n = 1536$ used here.

3.3. *Re_b-dependence*

To consider possible Pr-dependence at even higher Re_b, simulations A1 and A4 were continued at higher resolution and Reynolds number for approximately 7 forcing timescales. These simulations have $Re_b \approx 50$ at $Fr_f = 0.46$, with half the original viscosity $\nu = 0.06$ cm^2/s and increased resolution $n = 1920$. These simulations are reported as A1h ($Pr = 1, Fr_f = 0.46$) and A4h ($Pr = 8, Fr_f = 0.46$) in table 1. As discussed in section 3.2.2 for the lower Re_b simulations, a decrease in ϵ_p/ϵ_k as Pr increases from 1 to 8 is also found for $Re_b \approx 50$. However, the drop in this ratio as Pr goes from 1 to 8 is less at $Re_b \approx 50$ (24%) than at $Re_b \approx 30$ (39%).

Energy and buoyancy flux spectra from the higher-Re_b simulations are plotted in figure 17. The spectra are mostly consistent with the previous sections' results with respect to Pr-dependence. Kinetic energy spectra in figures 17(a,b) are minimally affected by the increase in Pr from 1 to 8, even less than what was seen with $Re_b \approx 30$ in figure 9(a). Potential energy spectra in figure 17(c,d) are far more sensitive than kinetic energy to Pr downscale of the Ozmidov scale and into the dissipation range. A longer plateau in the horizontal potential energy spectra, indicating a longer $k_h^{-5/3}$ scaling law range, is observed for $Pr = 8$ than for $Pr = 1$ past k_b and into the $k_h \in [k_O, k_d]$ subrange, which has been slightly widened in response to the larger Re_b. The buoyancy flux spectra show little influence from Pr outside of the restratification wavenumber ranges, as in the

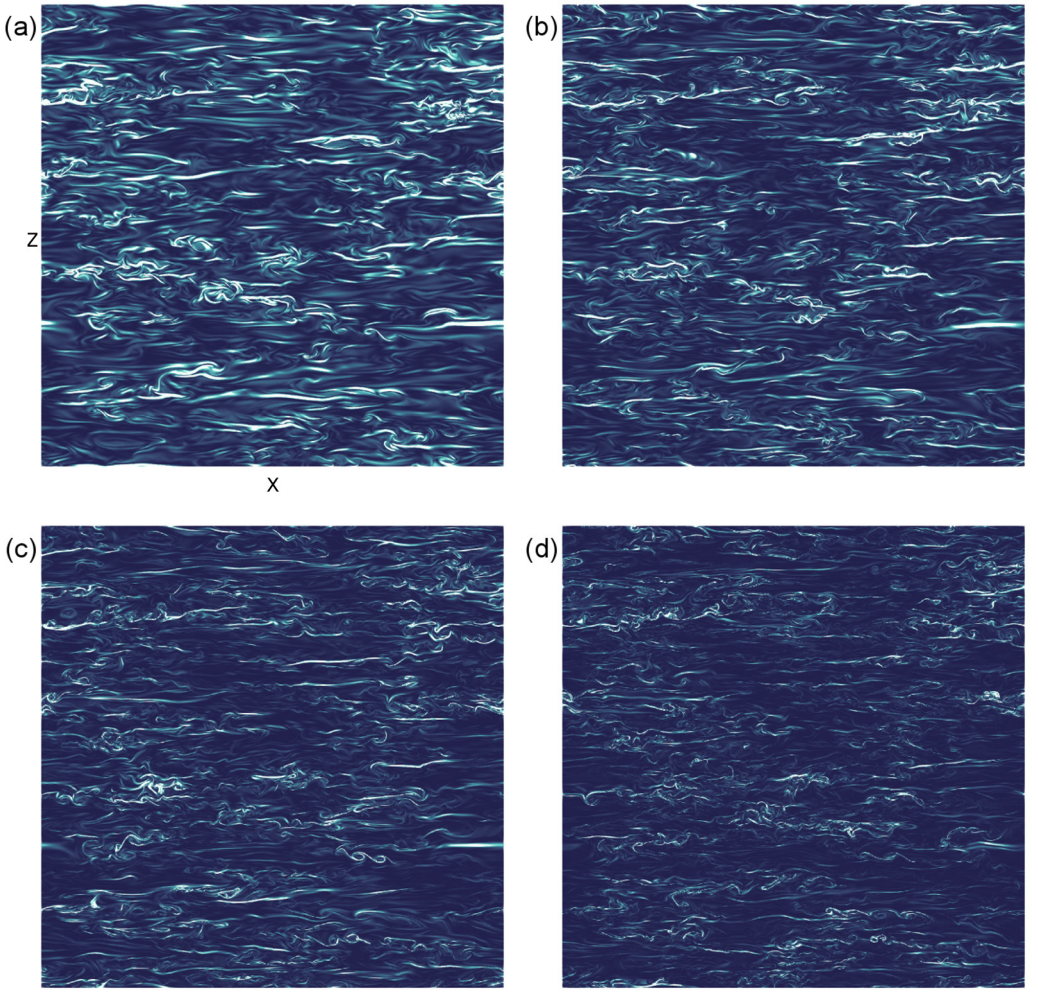

FIGURE 16. Vertical slices (x, z) at $y = 0$ of ϵ_p. Fixed $Fr_f = 0.12$ for (a) $Pr = 1$, (b) $Pr = 2$, (c) $Pr = 4$, (d) $Pr = 8$. The same colourmap is used for all panels as in figure 4(b), with the range modified for visibility across Pr.

previous buoyancy flux plots figures 12(a,b) at the same stratification, $Fr_f = 0.46$. As above, this restratification leads to a decrease in the ratio ϵ_p/ϵ_k as Pr increases from 1 to 8.

To compare the effect of Re_b on the examined energy spectra, ratios of $Pr = 8$ spectra to $Pr = 1$ spectra are computed for $Re_b \approx 30$ and $Re_b \approx 50$ and plotted in figure 18. We find that the kinetic energy spectra at and above the Kolmogorov scale, and therefore also at and above the Ozmidov scale, are less sensitive to changes in Pr as Re_b increases. Even as large wavenumbers where the ratio increases from one, ratio values for $Re_b \approx 30$ at a particular wavenumber are not realized in the $Re_b \approx 50$ case until a wavenumber that is greater by at least 100. Indeed, the ratio at k_d with $Re_b \approx 50$ is smaller than the ratio at k_d with $Re_b \approx 30$, especially in the horizontal wavenumber spectrum. This finding suggests that the kinetic energy spectra at scales at and above the Kolmogorov scale are

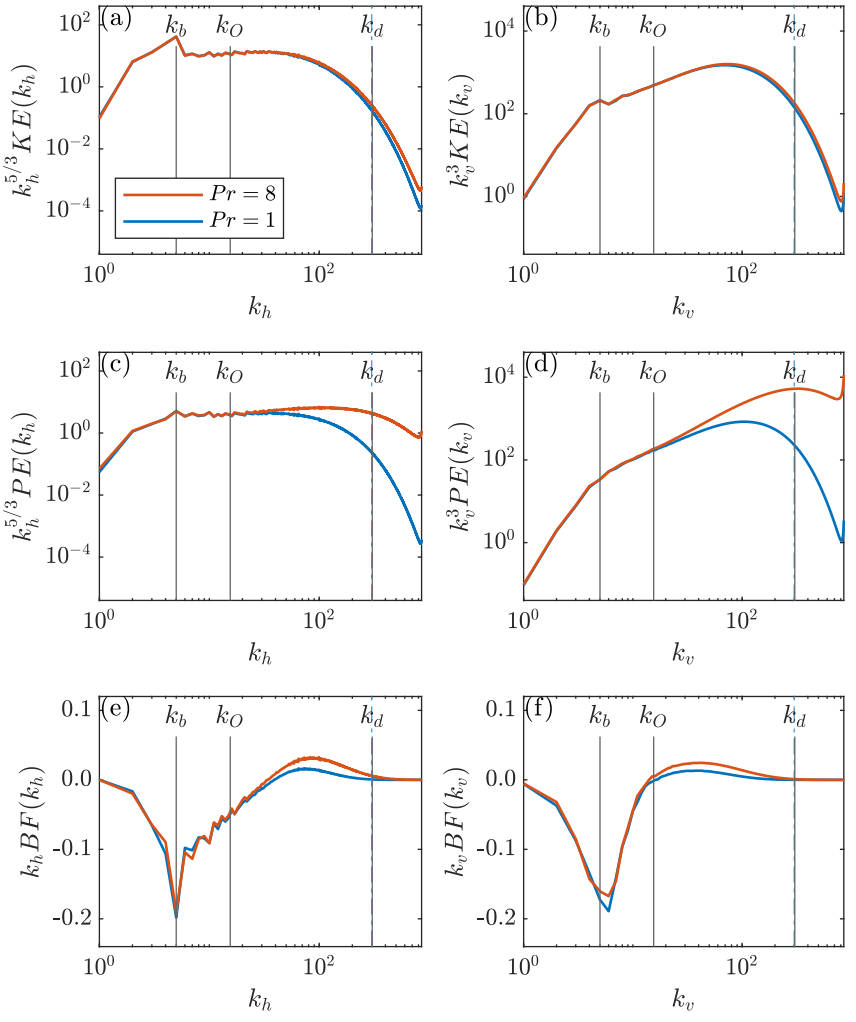

FIGURE 17. Compensated kinetic and potential energy spectra, and premultiplied buoyancy flux spectra for runs A1h ($Pr = 1$) and A4h ($Pr = 8$). Horizontal (left) and vertical (right) wavenumber spectra are shown. Vertical dash-dotted lines are k_B corresponding to Pr colours.

not very sensitive to Pr when $Re_b \approx 50$. By contrast, potential energy is different: figures 18(c,d) show that potential energy spectra are insensitive to Pr around and above the Ozmidov scale, but they are much more sensitive to Pr than the kinetic energy spectra around the Kolmogorov scale (a common vertical axis scaling is used for all four panels). Indeed, the potential energy spectra ratios at the respective k_d are approximately 10 for both values of Re_b, and show no evidence of decreasing with increasing Re_b.

Overall, we can draw a few conclusions about the potential for Pr-independence of stratified turbulence spectra at different Re_b. The potential energy is clearly the most sensitive to increases in Pr for all Re_b. The main effect of increasing Pr is increased potential energy at small scales, and associated enhanced positive buoyancy flux and restratification as a consequence of the increased potential energy and vertical motion permitted by larger Pr. Sensitivity to Pr is even observed upscale of the dissipative scales at all Re_b considered here. Much larger Pr may be needed to observe Pr-independence in the potential energy around the Kolmogorov scale. The potential energy spectra at the

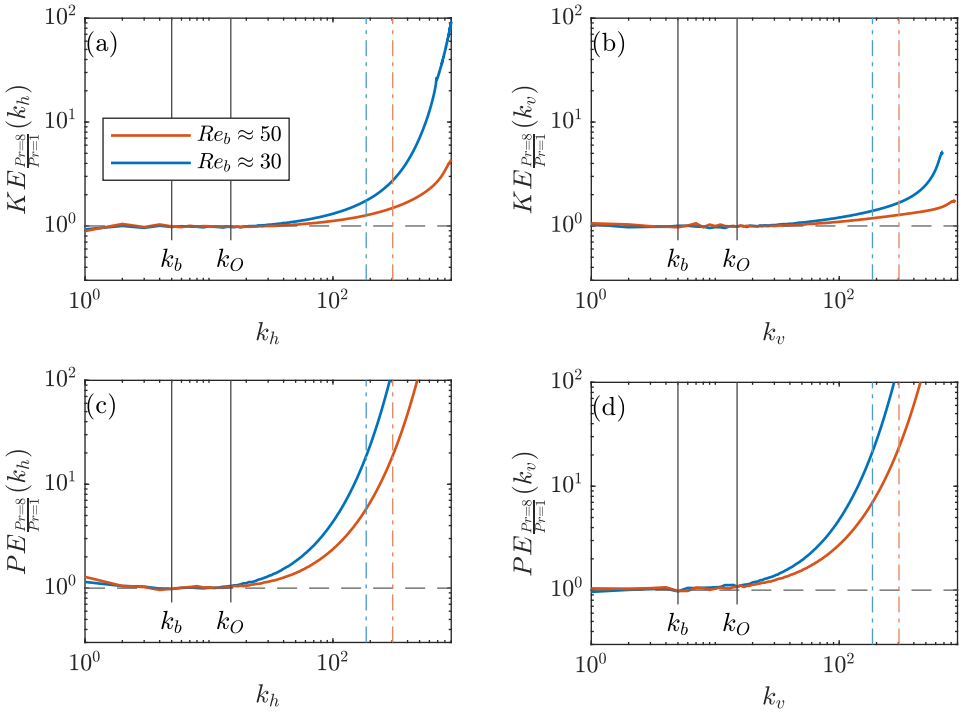

FIGURE 18. Ratios of $Pr = 8$ to $Pr = 1$ spectra for $Re_b \approx 30$ (runs A1, A4) and $Re_b \approx 50$ (runs A1h, A4h). Ratios of horizontal (left) and vertical (right) wavenumber spectra are shown. Vertical dash-dotted lines are k_d corresponding to Re_b colours.

Ozmidov scale, however, is far less sensitive to increases in Pr by $Pr = 8$, particularly for the larger values of $Re_b \gtrsim 8$ (simulation groups A and B), i.e. for a wide scale separation between the Kolmogorov and Ozmidov scales. As this scale separation increases with increasing Re_b, Pr-independence in the potential energy could possibly be reached at the Ozmidov scale for even smaller $Pr < 8$ with larger Re_b than considered here. On the other hand, the kinetic energy spectra are independent of Pr at and upscale of the Kolmogorov scale for Pr as small as 8, and as long as $Re_b > 1$. When Pr is increased from 4 to 8, the increase in buoyancy flux seems to be overcome by viscous dissipation so that the kinetic energy at these scales does not change much. Therefore, using $Pr = 8$ seems adequate to simulate larger Pr flows with $Re_b > 1$ as long as the main focus is on kinetic energy. For larger $Re_b \approx 30$, $Pr = 1$ is adequate as the kinetic energy spectra with $Pr = 1$ and $Pr = 8$ are very similar.

The buoyancy flux spectra with $Re_b \gtrsim 8$ also approach Pr-independence by $Pr = 8$ at the Ozmidov scale. However, for the large values of $Re_b \approx 30$ and 50, the positive peak in buoyancy flux in the restratification range (which sees the most Pr-sensitivity) occurs at scales smaller than the Ozmidov scale. As a result, the integrated buoyancy flux does not become independent of Pr for any Re_b considered here, which also suggests no Pr-independence in the ratio ϵ_p/ϵ_k or the mixing efficiency unless Re_b or Pr are even larger. For comparison, Okino & Hanazaki (2020) show that the buoyancy flux spectra are nearly unchanged between the $Pr = 70$ and $Pr = 700$ cases, suggesting that Pr-independence might be observed in the spectra for Pr as small as 70. Given that the decaying turbulence DNS in Okino & Hanazaki (2019, 2020) have a small $Re_b < 1$ for most of the integration time, it is possible that Pr-independence of the buoyancy flux,

and possibly also the mixing efficiency (or ϵ_p/ϵ_k), may be realized at a smaller $Pr < 70$ with larger Re_b where the separation between the Kolmogorov and Ozmidov scales is wider. Results from the present simulations show that the change in the related quantity ϵ_p/ϵ_k from $Pr = 1$ to $Pr = 8$ decreases as Re_b increases, which relates to a similarly smaller change in the integrated buoyancy flux. Additional simulations with $Re_b \gtrsim 30$ and larger Pr would be needed to reliably determine how buoyancy flux, ϵ_p/ϵ_k, and mixing efficiency is affected by Re_b, a relationship that is possibly non-monotonic (Salehipour *et al.* 2015).

4. Conclusions

Direct numerical simulations of stratified turbulence were performed to study the effect of varying Pr and to investigate the suitability for $Pr = 1$ simulations to reproduce $Pr \neq 1$ results. The simulations presented here employed random forcing of large-scale vortical modes on cubic domains. A fixed viscosity and a set of Fr_f were chosen to obtain a range of Re_b and Fr_h as Pr was varied. Spectra of kinetic energy, potential energy, buoyancy flux, kinetic energy flux, and potential energy flux were examined in fixed-Fr_f groups to identify scale-specific results dependent on Pr, and the effect of Re_b on Pr-sensitivity was briefly examined. Snapshots of the velocity, vorticity, temperature fluctuation, and potential energy dissipation fields in physical space were also visualized for a qualitative analysis of Pr-dependence.

When varying Pr, changes were naturally expected at very small scales, which is consistent with the change in k_B (k_d was nearly unchanged by Pr due to the fixed viscosity and forcing amplitude). Indeed, the most obvious Pr-dependence in the kinetic and potential energy spectra was found at large wavenumbers, where the potential and kinetic energy grew with Pr. The increase in energy can be explained by larger Pr permitting a wider wavenumber range of temperature fluctuations, possibly excited by enhanced inter-layer instabilities, which influence both kinetic and potential energy before viscous dissipation or buoyancy diffusion can occur. Since k_d was not changed much by Pr, the spectra of kinetic energy (and kinetic energy flux) were much less affected than potential energy (and potential energy flux). Subtle changes in the physical fields were found for different Pr, except of course in the potential energy dissipation field (figure 16). This was not unexpected, as Re_b was only slightly changed for a fixed Fr_f, so no change to the transition between stratified turbulence regimes was incurred by varying Pr.

Pr-dependence was found upscale of the dissipation range in most of the examined spectra. In some cases, this even extended upscale into the large-scale forcing interval, particularly in the horizontal wavenumber spectrum. Intermediate-to-large-scale Pr-dependence was visible more in the potential energy than kinetic energy spectra. The fully compensated energy spectra showed little Pr-dependence of the Kolmogorov constant, while the Obukhov-Corrsin constant was highly dependent on Pr, especially for stronger stratification. In the spectral kinetic energy flux, Pr-dependence was peculiar in that it only applied to k_h and k_v between the forcing interval and the dissipation range, where an inertial range could have existed if Re and/or Re_b were larger in these simulations. The spectral potential energy flux was extremely sensitive to Pr for most of the wavenumber range. The buoyancy flux spectra showed the strongest sensitivity to Pr in the restratification range just before k_d and k_B, but also exhibited some Fr_f-dependence. Following the description by Holloway (1988), it could be that for large Pr, the increased abundance of potential energy at these small scales even further amplifies the conversion back to kinetic energy.

Among all the examined spectra, the most strongly stratified $Fr_f = 0.058$ cases were very different from the three weaker stratifications. The simulations with $Fr_f = 0.058$ were the only cases in the $Re_b < 1$ regime; some of these observed differences may be consequences of the flow's transition to viscously coupled non-turbulent layers, as viscous and diffusive effects are expected when $Re_b \lesssim 1$, even at large horizontal scales due to vertical viscous and diffusive effects of the viscously-coupled layers. Breaks in the horizontal kinetic and potential energy spectra occurred at k_b associated with the suppression of the downscale energy cascade in this regime. The horizontal buoyancy flux spectra in figure 12(g) showed that the forcing scales were most affected by Pr, rather than the restratification range. In the spectral energy fluxes, $Fr_f = 0.058$ was unique in that $\Pi_K(k_h)$ was affected by Pr only at intermediate-to-large scales, and both $\Pi_P(k_h)$ and $\Pi_P(k_v)$ showed Pr-dependence for most of the wavenumber range. The $Fr_f = 0.058$ cases also exhibited negative horizontal kinetic energy flux at large scales, implying an upscale transfer of energy when stratification is especially strong. None of the spectral fluxes displayed any discernable range of constant flux at any Fr_f (except possibly $\Pi_K(k_v)$ at $Fr_f = 0.058$). The development of a true inertial range may have been hindered by the small Re and especially Re_b. The comparison between the $Re_b \approx 30$ and 50 simulations in section 3.3 (runs A1 and A4 versus runs A1h and A4h) show that at larger Re_b, the kinetic energy spectra tend to be less sensitive to changes in Pr, at least at scales around and above the Kolmogorov scale, which is reasonable given the weaker viscosity at $Re_b \approx 50$.

Given the impact of Pr upscale of the dissipation range, setting $Pr = 1$ to simulate realistic $Pr > 1$ flows appears to be reasonable when $Re_b \gtrsim 30$, when the focus is on kinetic energy at scales around and above the Kolmogorov scale. For smaller Re_b, at smaller scales, and for other quantities involving potential energy, $Pr = 1$ is not a suitable choice. Depending on Fr_f, Pr was shown to affect the examined spectra with varied severity and at unexpected scales. In particular, the spectral potential energy flux was especially sensitive to Pr, and was affected over more of its wavenumber range. For any investigation that might be reliant on accurately measured potential energy transfer, special care should be taken by properly computing these quantities using the appropriate Pr if possible. In addition, the ratio of potential to kinetic energy dissipation seems to be quite sensitive to Pr, even for Re_b up to 50.

The exhibited shallowing of energy spectra with increasing Pr was consistent with the results in Okino & Hanazaki (2017, 2020). Further, in all the examined quantities it was suggested there could be convergence to a limiting spectra shape as Pr increases, at least at scales around and above the Kolmogorov scale, as there was a declining growth in each spectra with larger Pr. That is, for Pr larger than 8 (but not extremely large as in Okino & Hanazaki 2017, 2020), and for large scales down to about k_d, it is expected that these examined spectra could converge to a shape not too different from the $Pr = 8$ case. Since varying Pr results in different k_B, it may only be at larger scales that convergence is possible. Okino & Hanazaki (2019, 2020) also note less of a difference in spectra between different Pr as these Pr increase beyond 1; Pr-independence could possibly be realized at some $Pr < 70$ in stratified turbulence for large Re_b ($Re_b \approx 50$ is not quite large enough). The kinetic energy and spectral kinetic energy flux did not exhibit major dependence on Pr, so performing DNS with $Pr = 1$ may be acceptable for those instances when large-scale kinetic energy is the main focus, as long as $Re_b \gtrsim 30$. However, the potential energy, buoyancy flux, and spectral potential energy flux might not exhibit similarly close convergence until a much larger $Pr > 8$. Performing simulations with an accurate Pr may be crucial to reliably study these quantities.

Additional simulations with $Pr > 8$ should be considered to further explore the extent

of the predicted convergence in all of the observed spectra, but would demand a higher resolution than $n = 1536$ used here. A wider range of Re_b as well as larger-Re simulations would allow for cases with identifiable inertial ranges to be studied. It may be of interest to explore any effects due to Pr on constant flux ranges, and to also see how restratification in the buoyancy flux spectra might change with more diverse cases. It would be very interesting to consider how results are (or are not) Pr-dependent when $Re_b \gtrsim O(100)$, however, the original challenge still remains: attainable values of Pr, Re, and Re_b will be limited by the available computational resources. For example, to perform a simulation with $Pr = 100$ with this setup, it is estimated that a resolution of $n \approx 5000$ would be needed for $k_{max}/k_B = 1$.

Future work on Pr-dependence of stratified turbulence could include the effects of rotation, which were neglected here. Based on the exhibited Pr-dependence of the buoyancy flux, the effect of Pr on mixing efficiency may be an interesting extension of the work here. Exploring the very small scales and looking into possible changes in intermittency due to Pr is also of interest. Ultimately, the dependence of the small-scale instabilities that develop between layers on Pr, and the potential role of Holmboe in addition to KH instabilities (e.g. Peltier & Caulfield 2003; Salehipour *et al.* 2016), should be investigated. The forced simulations presented here were varied in a limited way (only Fr_f and Pr were changed), but the code which produced them has many options to investigate stratified turbulence with different configurations. For example, one option could be to force fields other than the large vortical modes as shown here (e.g. velocity or temperature, possibly forcing large-scale gravity waves), or to modify some of the other forcing parameters.

Acknowledgements

This research was enabled in part by support provided by the Shared Hierarchical Academic Research Computing Network (SHARCNET), Compute/Calcul Canada, the Natural Sciences and Engineering Research Council of Canada (Grant No. RGPIN-386456-2015), and the Canadian Foundation for Innovation.

Declaration of Interests

The authors report no conflict of interest.

REFERENCES

Almalkie, S. & de Bruyn Kops, S. M. 2012 Kinetic energy dynamics in forced, homogeneous, and axisymmetric stably stratified turbulence. *Journal of Turbulence* **13** (29), 1–32.

Bartello, P. & Tobias, S. M. 2013 Sensitivity of stratified turbulence to the buoyancy Reynolds number. *Journal of Fluid Mechanics* **725**, 1–22.

Batchelor, G. K. 1959 Small-scale variation of convected quantities like temperature in turbulent fluid Part 1. General discussion and the case of small conductivity. *Journal of Fluid Mechanics* **5** (1), 113–133.

Billant, P. & Chomaz, J.-M. 2001 Self-similarity of strongly stratified inviscid flows. *Physics of Fluids* **13** (6), 1645–1651.

Bouruet-Aubertot, P., Sommeria, J. & Staquet, C. 1996 Stratified turbulence produced by internal wave breaking: two-dimensional numerical experiments. *Dynamics of Atmospheres and Oceans* **23** (1-4), 357–369.

Brethouwer, G., Billant, P., Lindborg, E. & Chomaz, J.-M. 2007 Scaling analysis and simulation of strongly stratified turbulent flows. *Journal of Fluid Mechanics* **585**, 343–368.

Burgers, J. M. 1948 A mathematical model illustrating the theory of turbulence. In *Advances in Applied Mechanics* (ed. R. von Mises & T. von Kármán), , vol. 1, pp. 171–199. Elsevier.

Carnevale, G. F., Briscolini, M. & Orlandi, P. 2001 Buoyancy-to inertial-range transition in forced stratified turbulence. *Journal of Fluid Mechanics* **427**, 205–239.

Caulfield, C. P. & Peltier, W. R. 2000 The anatomy of the mixing transition in homogeneous and stratified free shear layers. *Journal of Fluid Mechanics* **413**, 1–47.

Corrsin, S. 1951 On the spectrum of isotropic temperature fluctuations in an isotropic turbulence. *Journal of Applied Physics* **22** (4), 469–473.

Davidson, P. A. 2013 *Turbulence in Rotating, Stratified and Electrically Conducting Fluids*. Cambridge University Press.

Davidson, P. A. 2015 *Turbulence: An Introduction for Scientists and Engineers*. Oxford University Press.

de Stadler, M. B., Sarkar, S. & Brucker, K. A. 2010 Effect of the Prandtl number on a stratified turbulent wake. *Physics of Fluids* **22** (9), 095102.

Dewan, E. M. 1997 Saturated-cascade similitude theory of gravity wave spectra. *Journal of Geophysical Research: Atmospheres* **102** (D25), 29799–29817.

Durran, D. R. 2010 *Numerical Methods for Fluid Dynamics: With Applications to Geophysics*, *Texts in Applied Mathematics*, vol. 32. Springer.

Frigo, M. & Johnson, S. G. 2005 The design and implementation of FFTW3. *Proceedings of the IEEE* **93** (2), 216–231.

Gerz, T., Schumann, U. & Elghobashi, S. E. 1989 Direct numerical simulation of stratified homogeneous turbulent shear flows. *Journal of Fluid Mechanics* **200**, 563–594.

Gotoh, T. & Yeung, P. K. 2013 Passive scalar transport in turbulence: a computational perspective. In *Ten Chapters in Turbulence* (ed. P. A. Davidson, Y. Kaneda & K. R. Sreenivasan), pp. 87–131. Cambridge University Press.

Herring, J. R. & Métais, O. 1989 Numerical experiments in forced stably stratified turbulence. *Journal of Fluid Mechanics* **202**, 97–115.

Holloway, G. 1988 The buoyancy flux from internal gravity wave breaking. *Dynamics of Atmospheres and Oceans* **12** (2), 107–125.

Howland, C. J., Taylor, J. R. & Caulfield, C. P. 2020 Mixing in forced stratified turbulence and its dependence on large-scale forcing. *Journal of Fluid Mechanics* **898**.

Ishihara, T., Kaneda, Y. & Hunt, J. C. R. 2013 Thin shear layers in high Reynolds number turbulence DNS results. *Flow, Turbulence and Combustion* **91** (4), 895–929.

Kimura, Y. & Herring, J. R. 2012 Energy spectra of stably stratified turbulence. *Journal of Fluid Mechanics* **698**, 19–50.

Kolmogorov, A. N. 1941 The local structure of turbulence in incompressible viscous fluid for very large Reynolds numbers. *Doklady Akademii Nauk SSSR* **30**, 301–305.

Kundu, P. K., Cohen, I. M. & Dowling, D. R. 2012 *Fluid Mechanics*, 5th edn. Academic Press.

Lang, C. J. & Waite, M. L. 2019 Scale-dependent anisotropy in forced stratified turbulence. *Physical Review Fluids* **4** (4), 044801.

Laval, J.-P., McWilliams, J. C. & Dubrulle, B. 2003 Forced stratified turbulence: Successive transitions with Reynolds number. *Physical Review E* **68** (3), 036308.

Lilly, D. K. 1983 Stratified Turbulence and the Mesoscale Variability of the Atmosphere. *Journal of the Atmospheric Sciences* **40** (3), 749–761.

Lindborg, E. 2006 The energy cascade in a strongly stratified fluid. *Journal of Fluid Mechanics* **550**, 207–242.

Lindborg, E. & Brethouwer, G. 2007 Stratified turbulence forced in rotational and divergent modes. *Journal of Fluid Mechanics* **586**, 83.

Lucas, D., Caulfield, C. C. P. & Kerswell, R. R. 2017 Layer formation in horizontally forced stratified turbulence: connecting exact coherent structures to linear instabilities. *Journal of Fluid Mechanics* **832**, 409–437.

Maffioli, A. 2017 Vertical spectra of stratified turbulence at large horizontal scales. *Physical Review Fluids* **2** (10), 104802.

Maffioli, A., Brethouwer, G. & Lindborg, E. 2016 Mixing efficiency in stratified turbulence. *Journal of Fluid Mechanics* **794** (R3).

Maffioli, A. & Davidson, P. A. 2016 Dynamics of stratified turbulence decaying from a high buoyancy Reynolds number. *Journal of Fluid Mechanics* **786**, 210–233.

Okino, S. & Hanazaki, H. 2017 Turbulence in a fluid stratified by a high Prandtl-number

scalar. In *Sustained Simulation Performance 2017* (ed. M. Resch, W. Bez, E. Focht, M. Gienger & H. Kobayashi), pp. 113–121. Springer.

Okino, S. & Hanazaki, H. 2019 Decaying turbulence in a stratified fluid of high Prandtl number. *Journal of Fluid Mechanics* **874**, 821–855.

Okino, S. & Hanazaki, H. 2020 Direct numerical simulation of turbulence in a salt-stratified fluid. *Journal of Fluid Mechanics* **891**.

Ozmidov, R. V. 1965 On the turbulent exchange in a stably stratified ocean. *Izvestiya Akademii Nauk SSR* **1**, 861–871.

Peltier, W. R. & Caulfield, C. P. 2003 Mixing efficiency in stratified shear flows. *Annual Review of Fluid Mechanics* **35** (1), 135–167.

Riley, J. J. & de Bruyn Kops, S. M. 2003 Dynamics of turbulence strongly influenced by buoyancy. *Physics of Fluids* **15** (7), 2047–2059.

Riley, J. J. & Lelong, M.-P. 2000 Fluid motions in the presence of strong stable stratification. *Annual Review of Fluid Mechanics* **32** (1), 613–657.

Riley, J. J. & Lindborg, E. 2013 Recent progress in stratified turbulence. In *Ten Chapters in Turbulence* (ed. P. A. Davidson, Y. Kaneda & K. R. Sreenivasan), pp. 269–317. Cambridge University Press.

Rose, H. A. & Sulem, P. L. 1978 Fully developed turbulence and statistical mechanics. *Journal de Physique* **39** (5), 441–484.

Salehipour, H., Caulfield, C. P. & Peltier, W. R. 2016 Turbulent mixing due to the holmboe wave instability at high reynolds number. *Journal of Fluid Mechanics* **803**, 591–621.

Salehipour, H., Peltier, W. R. & Mashayek, A. 2015 Turbulent diapycnal mixing in stratified shear flows: the influence of prandtl number on mixing efficiency and transition at high reynolds number. *Journal of Fluid Mechanics* **773**, 178–223.

Siggia, E. D. 1981 Numerical study of small-scale intermittency in three-dimensional turbulence. *Journal of Fluid Mechanics* **107**, 375–406.

Smith, L. M. & Waleffe, F. 2002 Generation of slow large scales in forced rotating stratified turbulence. *Journal of Fluid Mechanics* **451**, 145–168.

Smyth, W. D. & Moum, J. N. 2000 Anisotropy of turbulence in stably stratified mixing layers. *Physics of Fluids* **12** (6), 1343–1362.

Smyth, W. D., Moum, J. N. & Caldwell, D. R. 2001 The efficiency of mixing in turbulent patches: Inferences from direct simulations and microstructure observations. *Journal of Physical Oceanography* **31**, 1969–1992.

Staquet, C. & Sommeria, J. 2002 Internal gravity waves: from instabilities to turbulence. *Annual Review of Fluid Mechanics* **34** (1), 559–593.

Stretch, D. D., Rottman, J. W., Venayagamoorthy, S. K., Nomura, K. K. & Rehmann, C. R. 2010 Mixing efficiency in decaying stably stratified turbulence. *Dynamics of Atmospheres and Oceans* **49**, 25–36.

Taylor, G. I. 1935 Statistical theory of turbulence. *Proceedings of the Royal Society of London, Series A* **151** (873), 421–444.

Tennekes, H. & Lumley, J. L. 1972 *A First Course in Turbulence*. MIT press.

Waite, M. L. 2011 Stratified turbulence at the buoyancy scale. *Physics of Fluids* **23** (6), 066602.

Waite, M. L. 2013 Potential enstrophy in stratified turbulence. *Journal of Fluid Mechanics* **722**.

Waite, M. L. 2014 Direct Numerical Simulations of Laboratory-Scale Stratified Turbulence. In *Modeling Atmospheric and Oceanic Flows: Insights from Laboratory Experiments and Numerical Simulations*, chap. 8, pp. 159–175. American Geophysical Union.

Waite, M. L. 2017 Random forcing of geostrophic motion in rotating stratified turbulence. *Physics of Fluids* **29** (12), 126602.

Waite, M. L. & Bartello, P. 2004 Stratified turbulence dominated by vortical motion. *Journal of Fluid Mechanics* **517**, 281–308.

Wyngaard, J. C. 2010 *Turbulence in the Atmosphere*. Cambridge University Press.